

We are IntechOpen, the world's leading publisher of Open Access books Built by scientists, for scientists

5,000

Open access books available

125,000

International authors and editors

140M

Downloads

Our authors are among the

154

Countries delivered to

TOP 1%

most cited scientists

12.2%

Contributors from top 500 universities



WEB OF SCIENCE™

Selection of our books indexed in the Book Citation Index
in Web of Science™ Core Collection (BKCI)

Interested in publishing with us?
Contact book.department@intechopen.com

Numbers displayed above are based on latest data collected.
For more information visit www.intechopen.com



Numerical and Experimental Analysis of Vibrations in a Three-Phase Linear Switched Reluctance Actuator

*José António da Costa Salvado,
Maria do Rosário Alves Calado and
António Eduardo Vitória do Espírito-Santo*

Abstract

This chapter focuses on the analysis and characterization of the vibrations produced by switched reluctance actuators. The emphasis stands on the linear configuration of this type of machine. The complexity of the mechanical system and the materials is used to define the modal frequencies. Moreover, the power controller topology, the excitation regimes, and the switching frequency used for the actuator operation can excite the natural modes and put restrictions on its usage. The analysis considers both numerical and experimental methodologies. The numerical technique relies on the finite element method (FEM) using the 3D model of the actuator to find its natural frequencies up to ~ 1.3 kHz. The experimental characterization counts on the operational modal responses and the acoustic noise emitted. We identify the regions of interest to measure the local accelerations and collect data for post-processing and record the audible noise emitted for signal analysis. The popular discrete Fourier transform and the joint wavelet-Fourier analysis are used for signal analysis. The reliability and the suitability of this approach are verified comparing both the numerical and the experimental outcomes and support the identification of the switching frequencies with high potential to excite the natural modes under the regular operation of the machine and to choose the proper control strategy.

Keywords: linear switched reluctance drives, force ripple, vibrations, acoustic noise, numerical analysis, operational modal responses, hybrid Spectrum

1. Introduction

Despite their simplicity, robustness, and reliability, switched reluctance drives face some limitations on their acceptance and usage due to the vibrations produced, and the acoustic noise emitted under operation. These are significant weaknesses and concerns and have been subject of research since the early 90s [1–5]. Several studies have been published focusing either on the origin of the vibrations or proposing methodologies to mitigate its effects by using the right control strategy, or on avoiding its presence at the design stage.

The principle of operation of switched reluctance drives, producing either rotational or linear movements, is based on the variation of the magnetic circuit reluctance, according to the relative position and the alignment of its fixed and moving parts [6]. The electromagnetic force ripple produced is the primary cause of vibrations. However, while in the rotational configuration, that is, the switched reluctance motor (SRM), the vibrations reveal stationary and periodic characteristics, for the linear switched reluctance actuator (LSRA), they tend to be nonstationary and confined to specific regions. That happens mostly due to the finite dimensions of the actuator parts and is related to wave propagation and reflection phenomena, as well as the geometry of the actuator and the properties of the materials.

This chapter addresses the modal analysis of the vibrations through the finite element method (FEM) and its evaluation and validation through experimental methods using the operational responses of the LSRA. The methodology is similar to operational modal analysis (OMA) and was considered due to the characteristics related to the operation of the actuator and its physical dimensions [7].

The LSRA considered in this research is a three-phase longitudinal magnetic flux actuator designed, built, and validated for precision positioning applications. **Figure 1** shows a general overview and the cross-section of the actuator. The LSRA dimensions in SI units are length: 2000 mm; width: 500 mm, height: 250 mm (includes the leveling feet), and weight: 47 kg. The actuator is built mainly with aluminum 6060-O (AlMgSi 0.5F25) profile frames forming the base assembly, two longitudinal aluminum 6060-O bars, and two ball guide rails made of chrome-plated steel, one per each side. Two aluminum plates on top of the structure are solidary bonded and constitute and constitute the moving platform. The platform has six steel ball runner blocks that fit into the ball rail guides and allow the longitudinal movement.

The parts belonging to the magnetic circuit, namely the poles of the primary and the teeth of the secondary, and the cores of the phase coils are made of carbon steel alloy S235 JR according to EN 10025 (ST37-2 under DIN 17100). Each coil is constituted by 1092 turns of AWG20 copper wire with a resistance of $\sim 10 \Omega$. **Figure 2a** shows a detailed view of the primary circuit, and **Figure 2b** shows a front view of one position with alignment in phase b . The magnetic circuit for each phase does not have shared cores or paths and therefore can be considered independent and the flux linkage constant.

According to the shapes of the poles and teeth, its alignment position, and the excitation current profiles, the attraction and thrust forces developed at the LSRA air gap can reach, respectively, 750 and 150 N (for $i_{as} = 4 \text{ A}$) [8]. Consequently, the operation of the LSRA is sensitive to ripple, namely for frequency values able to

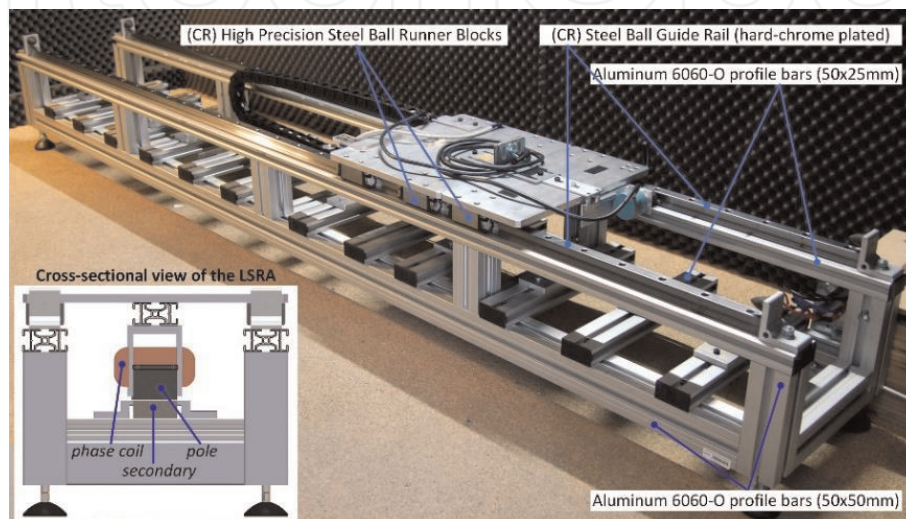


Figure 1.
Overview of the LSRA structure and details of its cross-section.

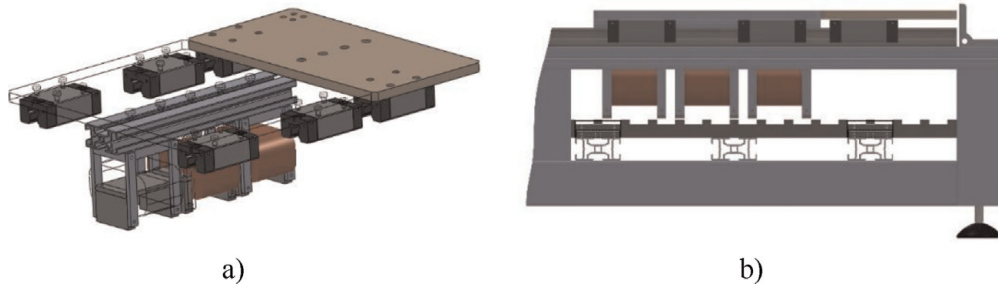


Figure 2. Detailed view of (a) the subassembly of the primary and (b) example of front view position of the translator with full alignment in phase b.

excite its natural modes. Moreover, the interactions between the electromagnetic motoring and the regenerative forces can also generate vibrations.

This chapter is organized as follows. Section 2 describes the operation basics of the LSRA, the power converter topology, the forces developed, and its relations with the origins of vibrations. The methods for dynamic analysis of mechanical systems are mentioned in section 3. Section 4 proposes the test setup and the configuration of instrumentation to perform the experimental tests for operational modal analysis. The analysis tools developed are also presented. Section 5 presents the results obtained, which are analyzed and discussed. Finally, the conclusion in section 6 summarizes the main achievements and contributions of this research work.

2. Operation of the LSRA

The principle of operation of switched reluctance machines is based on the variation of the magnetic reluctance according to the relative alignment positions of the poles and teeth of the primary and secondary, respectively, as shown in **Figure 3**.

The phase inductance, L_{as} , varies with the position, x_m , due to the longitudinal displacement along x , and reaches its maximum value with full alignment, being minimum at the unaligned position. By energizing phase a at the unaligned position (when the magnetic reluctance is maximum) with a coil current profile i_{as} , the work done by the developed electromagnetic forces tends to move the translator toward the aligned position where the inductance is maximum (minimum reluctance). The real current profile, i_{as} , tends to approach the ideal profile and is modeled by the switching signals, T_{a1} and T_{a2} , which depend on the switching technique, the power converter topology, and the control strategy adopted.

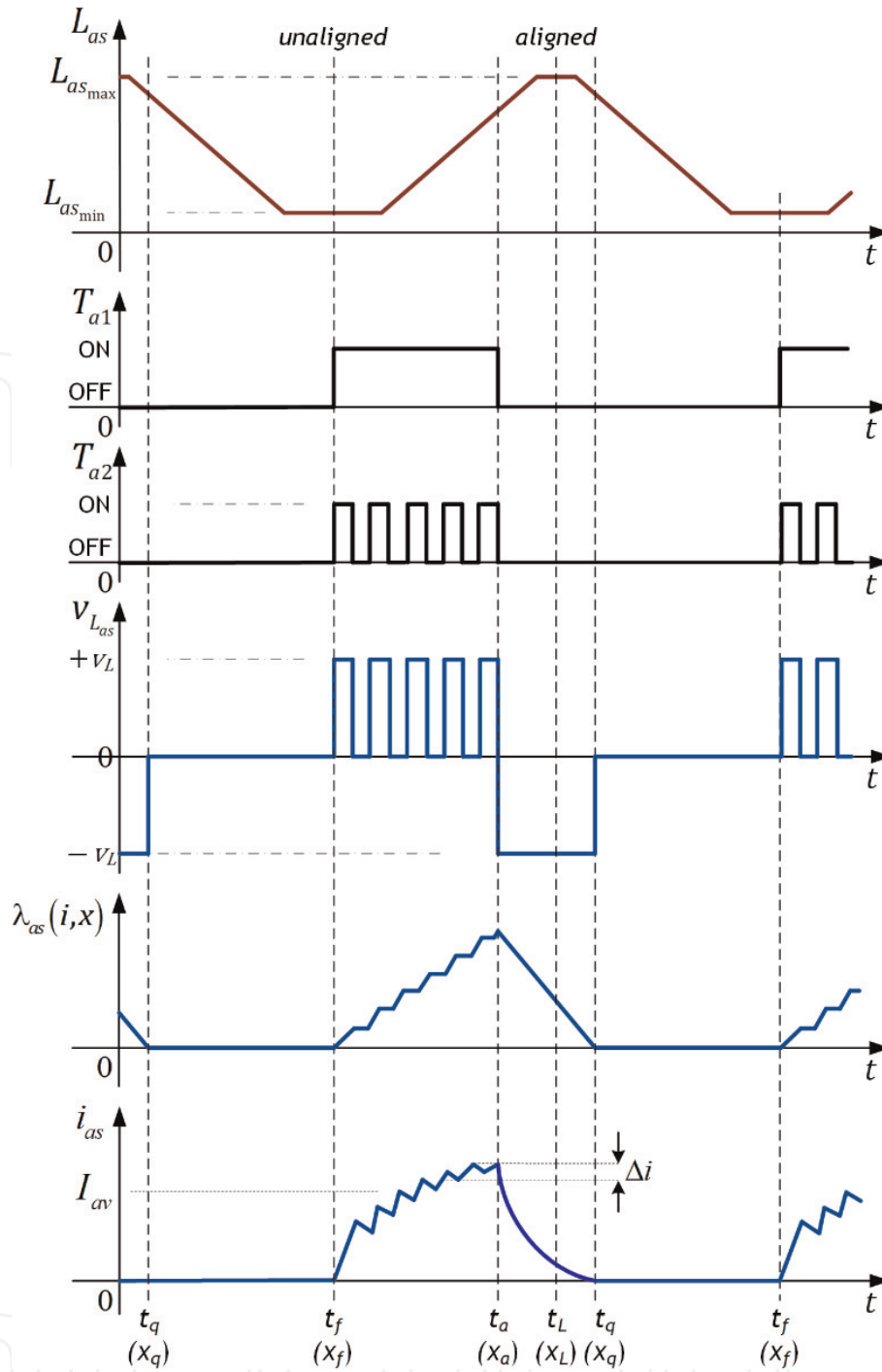
Due to the switching process, an induced electromagnetic force (emf) appears at the terminals of the phase coil. The induced emf can be expressed as

$$v_{La} = i_{as} \cdot \frac{\partial L_{as}(x_m, i_{as})}{\partial x} \cdot \frac{\partial x}{\partial t}. \quad (1)$$

The switching frequency, the duty cycle, and the control strategy used at the power converter define the phase current waveform. If the magnetic circuit has uniform geometry and the magnetic field is homogeneous, and neglecting the system losses, then, the linkage magnetic flux, λ_{as} , is proportional to the inductance and the current, according to expression

$$\lambda_{as}(x_m, i_{as}) = i_{as} \cdot L_{as}(x_m, i_{as}). \quad (2)$$

The magnetic energy stored in the coupling field depends on the inductance and the linkage flux. For linear and homogeneous systems with null initial linkage flux,


Figure 3.

Operation of phase α : variation of inductance with the position, time evolution of the switching control signals, time evolution of the voltage across the coil terminals, flux linkage and waveform of the phase current.

the electromagnetic energy associated with the field, W_{em} , is related to the variation of the magnetic flux linkage and also the current, and is expressed by

$$W_{em}(\lambda_{as}, x_m) = \int_{\lambda} i_{as}(\lambda_{as}, x_m) \cdot d\lambda_{as} = \frac{\lambda_{as}^2}{2 \cdot L_{as}(x_m, i_{as})}. \quad (3)$$

If the system can be considered homogeneous, and the flux linkage is uniform, the energy associated with the field in Eq. (3) is independent of the integration path. This means that the system is linear and conservative, and both, the mechanical and the electrical systems interact, and therefore, the variation of energy and

the system losses are uniform. Following these conditions, the variation of energy can be expressed in terms of partial derivatives with respect to its independent state variables as

$$dW_{em}(\lambda_{as}, x_m) = \frac{\partial W_{em}}{\partial \lambda_{as}} \cdot d\lambda_{as} + \frac{\partial W_{em}}{\partial x} \cdot dx = i_{as} \cdot d\lambda_{as} - f_{em} \cdot dx, \quad (4)$$

where, f_{em} is the electromagnetic motoring force.

If the coil excitation current is almost constant near its average value, $i_{as} \approx I_{av}$, then, using Eqs. (3) and (4), the attraction and motoring (traction) electromagnetic forces produced at the air gap, respectively, are given by

$$f_{ea} = \left. \frac{\partial W_{em}(\lambda_{as}, x_m)}{\partial z} \right|_{\lambda_{as}=C^{te}} = \frac{i_{as}^2}{2} \cdot \frac{dL_{as}(x_m, i_{as})}{dz} \quad (5)$$

and

$$f_{em} = \left. \frac{\partial W_{em}(\lambda_{as}, x_m)}{\partial x} \right|_{\lambda_{as}=C^{te}} = -\frac{i_{as}^2}{2} \cdot \frac{dL_{as}(x_m, i_{as})}{dx}. \quad (6)$$

Likewise, a regenerative force which tends to oppose movement is developed at the air gap and expressed as

$$f_{er} = -f_{em} = \frac{i_{as}^2}{2} \cdot \frac{dL_{as}(x_m, i_{as})}{dx}. \quad (7)$$

The switching frequency, the topology of the converter, and the control strategy cause variations in the coil excitation currents [9]. The controller used to activate the LSRA that supports the research described here is a three-phase half-bridge asymmetric power converter topology depicted in **Figure 4**, operating with a soft chopping control strategy, whose control signals, voltages, and currents relative to the operation of phase a are depicted in **Figure 3**.

These current variations foster ripple in the electromagnetic motoring and regenerative forces, whose interactions induce mechanical vibrations that can excite the natural modes of the LSRA. Therefore, knowledge of the natural structural frequencies of the actuator and its mode shapes is paramount.

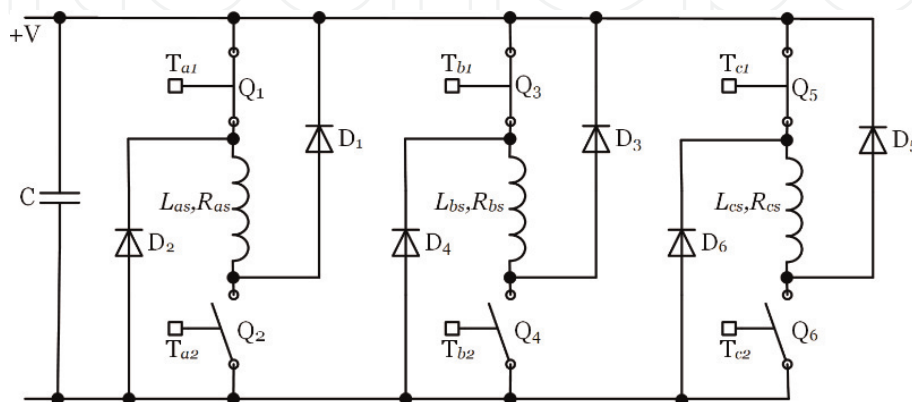


Figure 4. Electrical diagram representing the basis of operation of a three-phase asymmetric half-bridge converter in soft chopping mode.

3. Modal analysis via the finite element method

The vibrations and the acoustic noise problems in machinery depend on both the forces applied and structural aspects, namely, the system characteristics, the properties of the materials, and the boundary conditions. The diversity of sizes and shapes of its parts and their interconnections often leads to high-complexity mechanical models and multiple degrees of freedom (MDOF) systems.

Following the classical theories for structural dynamics analysis, systems are commonly described as a set of interconnected masses acting through a network of springs and dampers, with viscous damping, and submitted to a steady-state sinusoidal excitation by the action of the external forces, where the number of independent coordinates establishes the number of degrees of freedom.

3.1 Dynamic analysis for multiple degrees of freedom systems

The Lagrange's equation is an alternative approach to Newton's laws formulation that uses the equilibrium of energies in the system to describe its motion. Considering the kinetic and potential energies stored in the system, W_{kin} and W_{pot} , respectively, the condition of equilibrium is given by,

$$\frac{d}{dt} \cdot \frac{\partial(W_{pot} - W_{kin})}{\partial \dot{x}_i} - \frac{\partial(W_{pot} - W_{kin})}{\partial x_i} = 0 \quad i = 1, 2, \dots, n, \quad (8)$$

where x_i and \dot{x}_i represent, respectively, the generalized displacements and velocities at generalized coordinates i . The total kinetic energy stored in the springs due to compression and displacement Δx with respect to an initial position considers all coordinates i associated with the system [10]. For n-DOF systems, the Lagrange's equation is

$$\frac{d}{dt} \cdot \left(\frac{\partial W_{kin}}{\partial \dot{x}_i} \right) - \frac{\partial W_{kin}}{\partial x_i} + \frac{\partial W_{pot}}{\partial x_i} + \frac{\partial D_R}{\partial \dot{x}_i} = Q_i \quad i = 1, 2, \dots, n. \quad (9)$$

Here, D_R is the Rayleigh's dissipation function representing the energy losses at the dumpers, and Q_i refers to the generalized non-conservative forces. For each element of order i , the quadratic forms of the kinetic and potential energies and the Rayleigh's dissipation function can be expressed in matrix notation as

$$W_{kin} = \frac{1}{2} \cdot \dot{\mathbf{x}}^T \cdot \mathbf{M} \cdot \dot{\mathbf{x}}, \quad (10)$$

$$W_{pot} = \frac{1}{2} \cdot \mathbf{x}^T \cdot \mathbf{K} \cdot \mathbf{x}, \quad (11)$$

$$D_R = \frac{1}{2} \cdot \dot{\mathbf{x}}^T \cdot \mathbf{C} \cdot \dot{\mathbf{x}}. \quad (12)$$

Here, \mathbf{M} , \mathbf{C} , and \mathbf{K} are square and symmetric matrices that represent the inertia (mass), and the damping and stiffness coefficients, respectively; \mathbf{x} and $\dot{\mathbf{x}}$ are the vectors of generalized displacements and velocities. The off-diagonal coefficients of matrices \mathbf{M} , \mathbf{C} , and \mathbf{K} are the coupling terms that depend on the configuration of the system and its dimensions depend on the number of degrees of freedom.

Considering small-amplitude displacements with reference to the equilibrium points, that is, $x_i \approx x_{ei}$, the Lagrange's equation can be linearized and expressed using matrix notation in the form

$$\mathbf{M} \cdot \ddot{\mathbf{x}}_i + \mathbf{C} \cdot \dot{\mathbf{x}}_i + \mathbf{K} \cdot \mathbf{x}_i = \mathbf{Q}_i. \quad (13)$$

Finding the solutions of Eq. (13) for MDOF systems with several parts, of several dimensions and shapes and interconnections, often requires considerable computational time and powerful numerical tools. Therefore, a common approach consists of performing the modal analysis using the finite element method (FEM).

3.2 Modal analysis via the finite element method

The free vibration result for undamped systems is labeled as mode and corresponds to a standing wave where all points move at one frequency, that is, the natural frequency, with a particular phase relation. Consequently, for any mode of order r , the eigenvalue, ξ_r , corresponds to the undamped natural frequencies and the eigenvectors, $\boldsymbol{\psi}_r$, contain information on the mode shapes associated with these frequencies. As modes have a weighted orthogonality property [10] (pp. 309–310) and, the mass, stiffness, and damping matrices are in general Hermitian, it is possible to perform matrix diagonalizations and obtain their eigenvectors, therefore simplifying the problem. Hence, in real systems, one can consider proportional damping as a linear combination of the mass and stiffness matrices and perform the decoupling of MDOF systems into modal coordinates [11]. Thus, it is possible to represent the motion by rewriting Eq. (13) and obtain

$$\mathbf{M}_r \cdot \ddot{\mathbf{x}}_i + \mathbf{C}_r \cdot \dot{\mathbf{x}}_i + \mathbf{K}_r \cdot \mathbf{x}_i = \boldsymbol{\psi}_r^T \cdot \mathbf{Q}_i. \quad (14)$$

where

$$\mathbf{M}_r = \boldsymbol{\psi}_r^T \cdot \mathbf{M} \cdot \boldsymbol{\psi}_r, \quad (15)$$

$$\mathbf{K}_r = \boldsymbol{\psi}_r^T \cdot \mathbf{K} \cdot \boldsymbol{\psi}_r, \quad (16)$$

$$\mathbf{C}_r = \alpha \cdot \mathbf{M}_r + \beta \cdot \mathbf{K}_r = \boldsymbol{\psi}_r^T \cdot \mathbf{C} \cdot \boldsymbol{\psi}_r. \quad (17)$$

Each row in Eq. (14) corresponds to a single-degree of freedom (SDOF) system whose equation of motion considers its modal parameters: mass, damping, and stiffness. The undamped natural frequency and the damping coefficient for mode r , respectively, are given by

$$\omega_r = \sqrt{\frac{k_r}{m_r}}, \quad (18)$$

$$c_r = -2 \cdot \sigma_r \cdot m_r, \quad (19)$$

where k_r and m_r are the stiffness constant and mass, respectively, and c_r is the damping coefficient.

The use of Lagrange's equation to MDOF systems is possible by selecting a set of independent coordinates and applying successive differentiation along each coordinate. Hence, the analysis via FEM corresponds to decomposition into many building blocks to find the approximate solutions of the differential equations that describe the model. This process corresponds to a system discretization technique. Moreover, it allows the collection of the complete system responses as linear combinations of the set of responses from numerous single degree of freedom systems.

3.3 Results from FEM simulations

Most parts of the LSRA in **Figure 1** are uniform plates, and uniform bars mounted either transversely or longitudinally. However, the multiplicity of parts, their shapes and configurations and its interconnections, the diverse materials used, and the geometry increase the complexity of the system. That leads to the use of FEM simulation tools as an efficient approach for analysis of the natural modes and the vibration frequencies of the LSRA structure.

Based on the LSRA dimensions and symmetry characteristics, five scenarios are considered according to the position of the translator, which correspond to configurations P1–P5, as shown in **Figure 5**. For the requisites of experimental modal excitation analysis, five positions are established to apply excitation from external forces: E1–E5.

Based on these configurations and the materials used in the real actuator, we used SolidWorks to design the 3D model for each LSRA configuration (P1–P5) and built-in simulation tools to perform the FEM-based modal analysis study. The global contacts are considered ideal and set as bonded with no clearance and no penetration among parts. To optimize the simulation results, we use:

- curvature-based mesh, Jacobian, tetrahedral elements (four points);
- fine-density mesh, with elements of size among 1.2 (min) and 12 mm (max); and
- growth ratio of 1.6 per element, and at least eight elements to describe circles.

These simulation arrangement presets lead to a high-quality mesh, whose detailed view is presented in **Figure 6**. With this mesh configuration, the total number of elements is $\sim 1,221,800$ of which 28% have an aspect ratio less than 3, and 8% have an aspect ratio greater than 10. The number of nodes is around 2,226,200, hence achieving $\sim 6,678,600$ degrees of freedom for 3D coordinates.

To complete the modal analysis study, we selected the FFEplus solver embedded in SolidWorks software simulation tools and performed the frequency analysis for each scenario in the range up to 1.3 kHz. The FFEplus solver adopts an iterative integration method to find the solutions and evaluates the error for each iteration; when the latter is small enough, the result is assumed stable. When compared to the direct method, this approach leads to gains in accuracy but with higher computational costs. For example, for each configuration model, the iterative process requires around 30 hours for mesh construction and analysis, on a PC with Intel

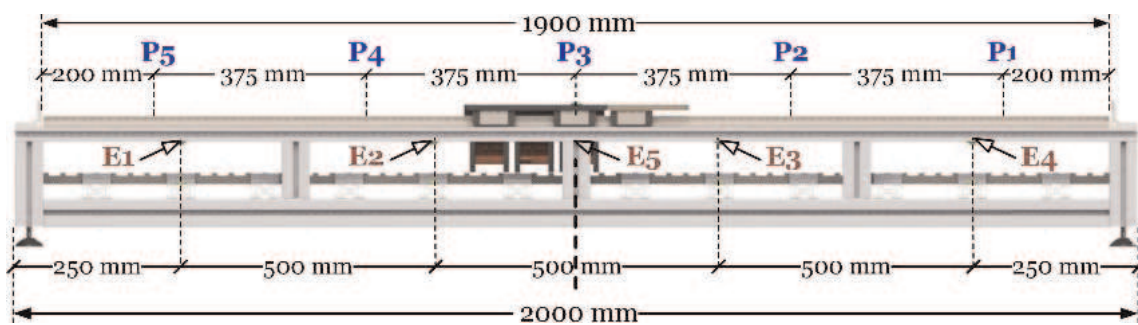


Figure 5. Detailed view of the configurations considered for experimental tests: positions of the translator (P_x) and points to apply external excitation forces (ex).

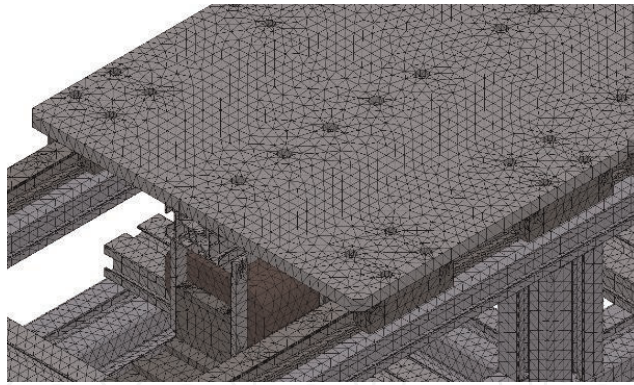


Figure 6.
 Detailed view of the mesh and tetrahedral elements for FEM analysis.

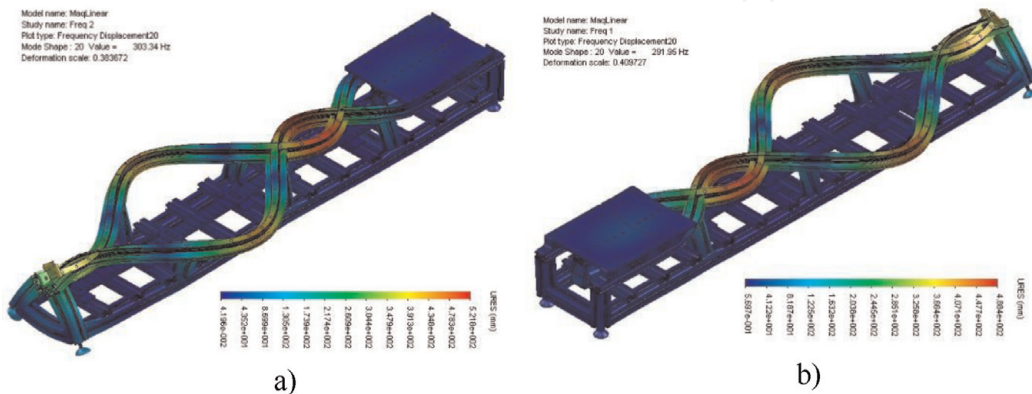


Figure 7.
 Modal shapes for mode #20: (a) at position P1 ($f_n = 303$ Hz) and (b) at position P5 ($f_n = 292$ Hz).

Core 2 Duo E7500 CPU @ 2.93 GHz, 6 GB RAM DDR3 @ 1.333 Mbps (36 ns) and Windows 7 Pro 64-bit operating system.

The modal analysis results for each 3D model reveal a set of 80 natural modes from which the first six frequencies correspond to rigid body vibration modes, as expected. Accordingly, modes of order 7 correspond to the first useful natural modes, in a set of 74 significant modes whose complete list and the corresponding analysis are made in [12]. Here, we only present a brief summary of the results obtained and show a few examples of the modal shapes.

For all configurations considered and for same-order modes, the vibration frequencies are close to each other. On the other hand, for sequential modes at one configuration, the differences in frequency are small. The average modal frequency interval is ~ 15 Hz with minimum differences as small as 1 or 2 Hz (e.g., for modes 41 and 42 or modes 57 and 58 at P1). Moreover, for adjacent modes, the modal frequencies can have very close values meaning that a given vibration frequency can be excited for different modes in different actuator configurations.

Because each mode corresponds to a dominant vibration with displacement at specific parts or subassemblies, it is imperative to look also at the modal shapes. **Figure 7a** and **b** illustrates the mode shapes associated with mode #20 for positions P1 and P5, respectively, whose frequencies are ~ 303 Hz and ~ 292 Hz.

The mode shapes at positions P1 and P5 are symmetric and reveal displacements at the top bars associated with elastic waves in phase opposition. It must be noted that the movements shown at these images are not at the correct scale, serving merely to illustrate the most significant displacements for each mode. **Figure 8a** and **b** shows the counterpart and symmetric modal shapes for P3 corresponding to modes #13 (~ 226 Hz) and #14 (~ 230 Hz), correspondingly. Although with different-order modes, the modal shapes are similar, and frequency values are close.

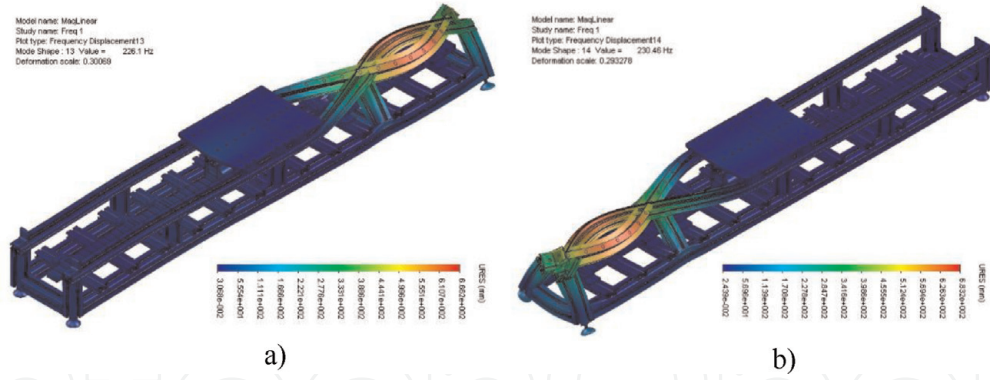


Figure 8. Modal shapes at position P3: (a) mode #13 ($f_n = 226$ Hz) and (b) mode #14 ($f_n = 230$ Hz).

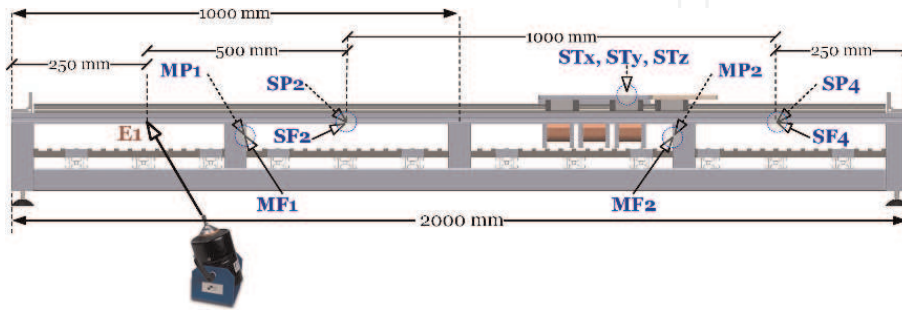


Figure 9. Detailed view of the configurations and instrumentation considered for the experimental modal excitation tests.

At position P3, the length of the bar's segments is identical on both sides, but the center of mass is not aligned with the symmetry axis. That influences the symmetric characteristic of the vibration modes, namely the shapes of its deformation waves. Hence, while the mode shapes of first-order modes (modes 13 and 14) exhibit symmetry, the second-order modes show anti-symmetric mode shapes. These characteristics apply to other modes at P3.

3.4 Experimental modal excitation

The modal frequencies were evaluated through experimental modal excitation. For that purpose, we used an electrodynamic shaker to apply the external forces at excitation points E1–E5, and several accelerometers are placed along with the structure of the actuator, as shown in **Figure 9**.

The accelerometers are installed over a layer of bee wax with ~ 0.5 mm thickness at the areas with significant displacement: two at the top longitudinal bar at the front side (positions SF n); two at the opposite face (positions SP n); and four accelerometers at middle vertical bar; two at the front side and other two at the rear (positions MF n and MP n , respectively). All these accelerometers have one-axis sensitivity (ADXL001-70Z). Moreover, one three-axis accelerometer (ADXL326Z) is mounted on top of the translator plate, to measure the vibrations along the X-, Y-, and Z-axis (ST x , ST y , and ST z , respectively).

4. Operational modal responses

The modal frequencies whose mode shapes denote vertical displacement are of interest for analysis, due to their potential for excitation during the regular operation of the LSRA. To evaluate the operational modal responses, we measure the local

accelerations at the structure. To achieve this objective, we establish a test setup and define the experimental procedures. To collect data of the local responses, we designed and developed a modular data acquisition system and developed specific analysis tools.

4.1 Experimental setup and instrumentation

The experimental setup is formed by the actuator, the half-bridge power converter, power supply units, regular equipment for test and measurement (oscilloscope, multimeter, and function generator), a host PC and a modular, and distributed system for data acquisition (MDSAM) to measure the local responses and collect data from sensors [13, 14]. The instrumentation set is composed by accelerometers placed at selected positions of the LSRA structure. Due to the symmetry characteristics of the actuator, only half of the structure needs to be instrumented for data collection. **Figure 10** shows the locations of 10 one-axis ratiometric accelerometers with analog output response (voltage) and ± 70 g sensitivity (ADXL001-70Z), placed at the left side of the structure with the translator at configuration P2.

The accelerometers are also installed over bee wax with ~ 0.5 mm thickness with the following distribution criteria: four at the front side on the top longitudinal bar (positions SF n); four at top longitudinal bar on the opposite face (positions SP n); and two accelerometers mounted at the bar that constitutes the secondary of the actuator (SS1 and SS2). The three-axis accelerometer (ADXL326Z) is mounted on top of the translator plate, to measure the vibrations along the axes X, Y, and Z (ST x , ST y , and ST z , respectively). The phase current is evaluated by using current sensors and oscilloscope probes to monitor its waveforms; an ampere meter is also used to measure the average current values. The accelerometers connect to the MDSAM through the intelligent and interface modules based on 16-bit low-power microcontrollers (MSP430F5419 or MSP430F5438), and anyone of the 13 output terminals from the accelerometer modules corresponds to one measurement channel of the MDSAM. The intelligent sensor modules communicate with the host PC through a USB 2.0 bus, and the MDSAM is fully controlled through the host PC via MATLAB environment.

To conduct the operational modal tests, the translator is fixed and locked at configuration P2, in a position that corresponds to 50% alignment between poles and teeth, as depicted in **Figure 11a**. To produce the electromagnetic excitation forces, we consider exclusively the activation of phase a , whose coil current is fed by the asymmetric half-bridge converter operating at soft chopping switching strategy. The soft chopping operation mode is achieved by setting ON the control signal T_{a1} , while T_{a2} is adjusted to a given switching frequency— f_{Ta2} —and a duty cycle of $d = 85$ % (see **Figures 3** and **4**). This configuration allows an average phase

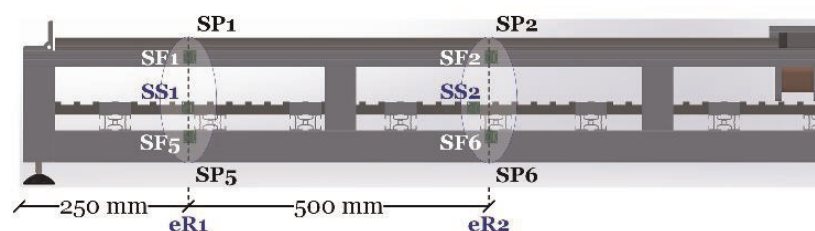


Figure 10. Placement of accelerometers at the left half of the LSRA structure for local response measurements with translator positioned at P2.

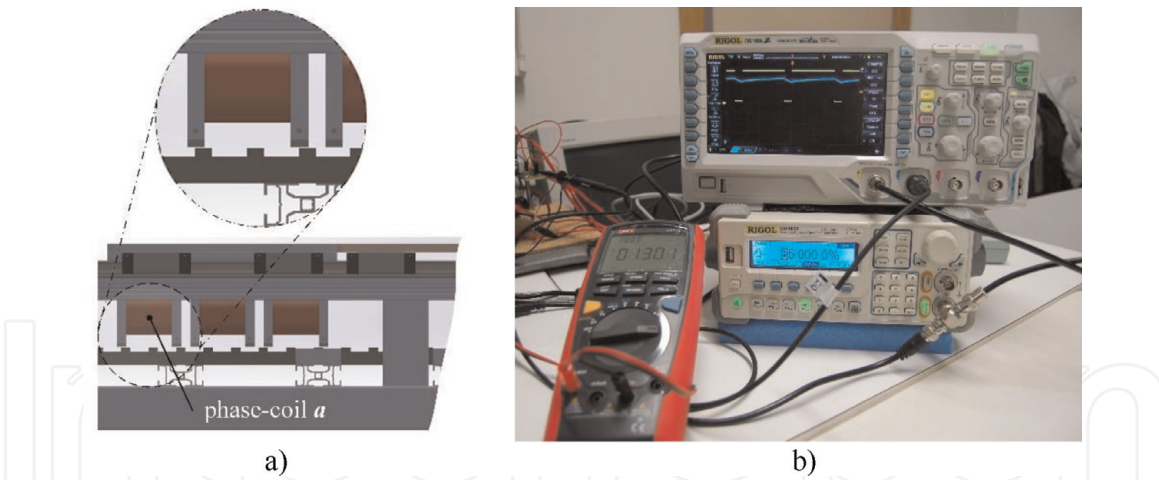


Figure 11. Detailed view of (a) the magnetic circuit with 50% alignment, and (b) test bench setup to measure the current in phase a ($I_{av} = 1.3 \text{ A}$ @ $d = 85\%$).

current of 1.3 A through the phase coil when a 30 V voltage is used for phase activation, as shown in **Figure 11b**.

The 50% alignment and this phase current profile generate an electromechanical traction force of approximately 30 N, whose work tends to move the translator toward the full alignment position. However, as the translator is locked, and due to the nature of the forces generated, the excitation forces act similarly as hammer impacts with periodic steady state [7].

4.2 Analysis of stationary and nonstationary signals

The data collected through the MDSAM are organized according to the type of sensor and with correspondence to the point of measurement. The data obtained from one measurement set are stored in MAT-files (*.mat) for further processing. After reading, extracting data from the selected MAT-file, and identifying the type of response associated to the signal (phase current or local acceleration), the user establishes the parameters for analysis and defines the desired representation, either the time response or the spectrum. For that purpose, we developed a set of MATLAB scripts and functions for MDSAM control, data acquisition, and storage and for signal analysis of the local responses. The signal analysis tools are also based on MATLAB and use the windowed discrete Fourier transform (DFT), whose coefficients can be calculated through Eq. (20). The options of window function include Rectangular, Hamming, Hann, Bartlett, and Flat-Top, selected according to their performance and suitability for this application [15]. The DFT is a popular solution that performs quite well for stationary signals and therefore is used in a vast number of applications.

However, in LSRA, the vibrations are in most cases localized and characterized by nonstationary signals, due to an eventual mixture with other vibration frequencies associated with other neighboring parts. Hence, the localization and nonstationary characteristics of the vibrations in LSRA demand innovative approaches and specialized tools for signal analysis, rather than merely the Fourier analysis methods.

An alternative for signal analysis is the discrete wavelet transform (DWT) which has proper localization in the frequency domain and whose basis functions are orthogonal and scalable in the time domain. The most prevalent wavelet constructions include the Daubechies family of orthogonal wavelets with n vanishing

moments (DBn) and the Cohen-Daubechies-Feauveau (CDF) family of biorthogonal wavelets. The DWT can be implemented through banks of finite impulse response (FIR) filters, thus allowing signal analysis with multiresolution [ref] as shown in **Figure 12**.

The left-hand side of **Figure 12** represents a multiresolution scheme that uses low-pass, \tilde{h} , and high-pass, \tilde{g} , analysis filters to obtain the DWT coefficients. Each stage l of decomposition consists of obtaining the approximation, $a_{l,n}$, and the detail coefficients, $d_{l,n}$, resulting from the low-pass and high-pass filtering of the signal, and applying a decimation factor of 2 for in-place computation. The first frequency band of the signal is organized in octaves where the lower band contains a smooth representation of the signal; the following bands contain the details with scaled resolution. Successively applying the analysis filters to the detailed coefficients in each level leads to a wavelet packet (WP) decomposition scheme as depicted at the right-hand side in **Figure 12**, also known as wavelet packet analysis (WPA). Using this scheme and for l levels of analysis, the initial bandwidth is divided into 2^l regularly distributed bands. Hence, both the DWT and WPA schemes are suited for the analysis of nonstationary signals with adjustable resolution.

4.3 Software tools for signal analysis and representation

Specific and dedicated software tools were developed by the authors in MATLAB using built-in and custom functions to perform the analysis of the results obtained from experimental modal excitation and from the operational modal responses.

The flowchart of **Figure 13** shows the sequence of actions for the analysis of the local responses whose data are stored in *.mat files. Through a dialog box, the user chooses the file, and the relevant data are extracted, namely the arrays containing the data of each channel. Then, each array is processed according to the type of data and the desired analysis following a control order: “A” for audio; “V” or “T” for accelerations.

The analysis of signals using the Fourier method and its spectral representation is obtained through the discrete Fourier transform (DFT), expressed as,

$$X_w[q] = \sum_{n=0}^N \{x[n] \cdot w[n]\} \cdot e^{-j\frac{2\pi nq}{N}}, \quad 0 \leq q \leq N - 1 \quad (20)$$

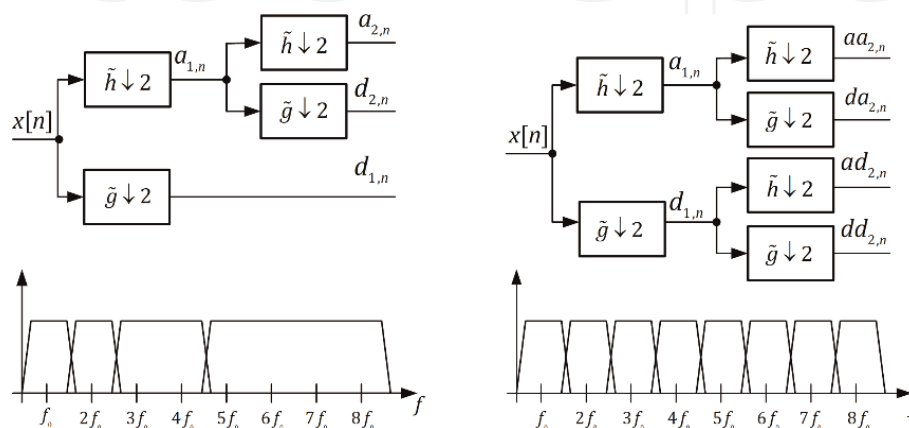


Figure 12. Diagrams for two-level multiresolution signal analysis via DWT (left) and through wavelet packet decomposition (right).

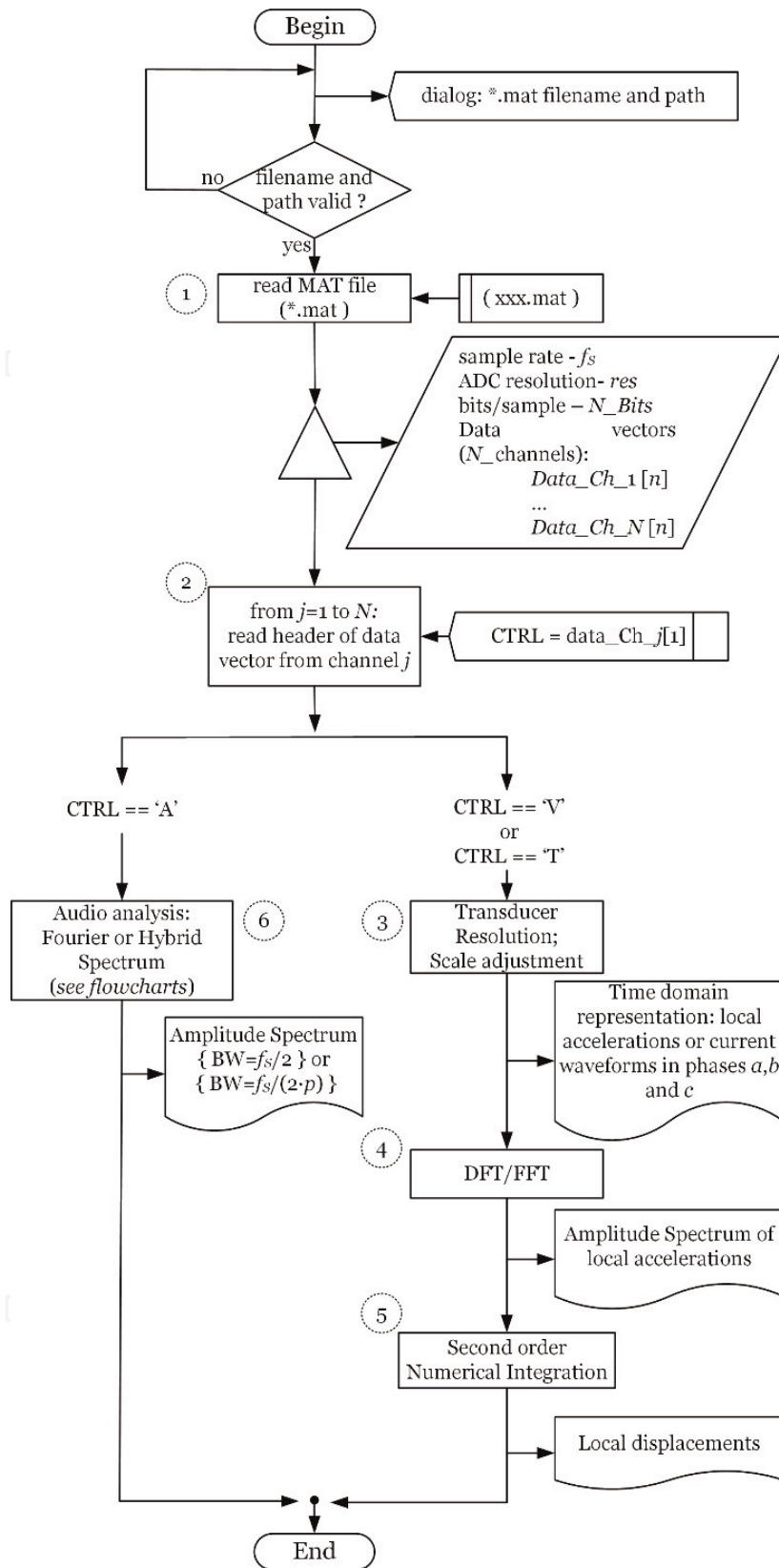


Figure 13.
Description of the tool developed for signal analysis.

where $x[n]$ is the discrete-time signal and $w[n]$ is the finite length window function of size N and defined within the interval $0 \leq n \leq N - 1$. The same is possible via the fast Fourier transform (FFT). The flowchart of **Figure 14** illustrates the sequence of actions corresponding to the DFT or FFT and the amplitude spectrum of the responses, either for the accelerations, phase currents, or audio signals. This sequence is activated at stage 6 at the flowchart of **Figure 13**.

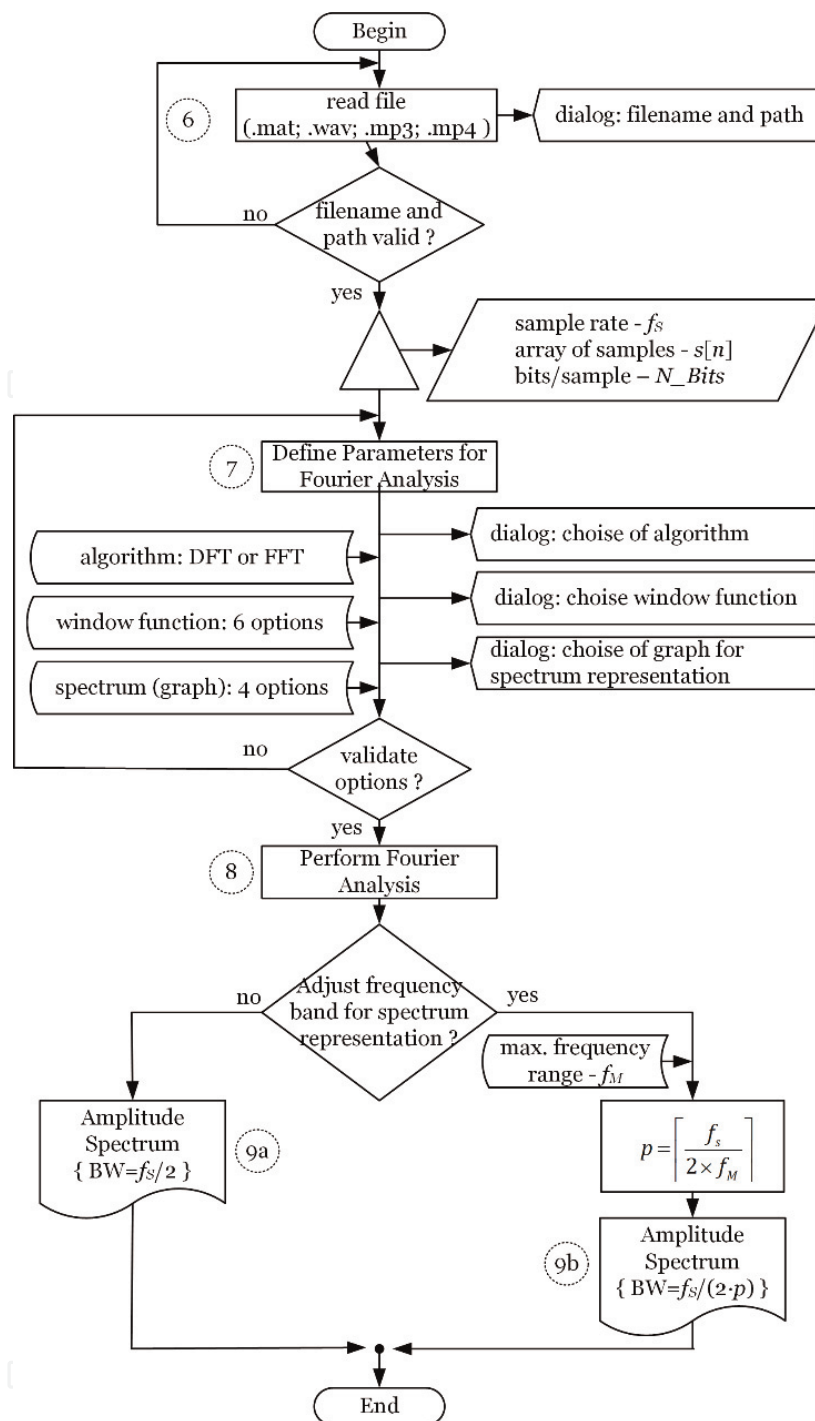


Figure 14. Flowchart illustrating the operation of the Fourier analysis tool.

The window function is chosen among six options: rectangular, Hann, Bartlett, Hamming, Bartlett-Hann, and Flat-Top. With exception to the rectangular window, which is suited for impact test analysis, the remaining functions are suited for periodic excitation. By default, the Hann window is used. The options for spectrum representation permit four graphic types: amplitude vs. frequency using linear scales; a variant with amplitude scale in dB; and the same options but using semi-logarithmic scales. In any case, the frequency range is adjustable. By default, it uses the signal bandwidth. However, due to the nonstationary characteristics of the vibrations associated with the operation of the LSRA, an alternative analysis method is available. This technique, which combines wavelet and Fourier analyses to represent the hybrid spectrum, is described in the flowchart of **Figure 15**. After selecting the file and data extraction, the user establishes the parameters for WPA, namely

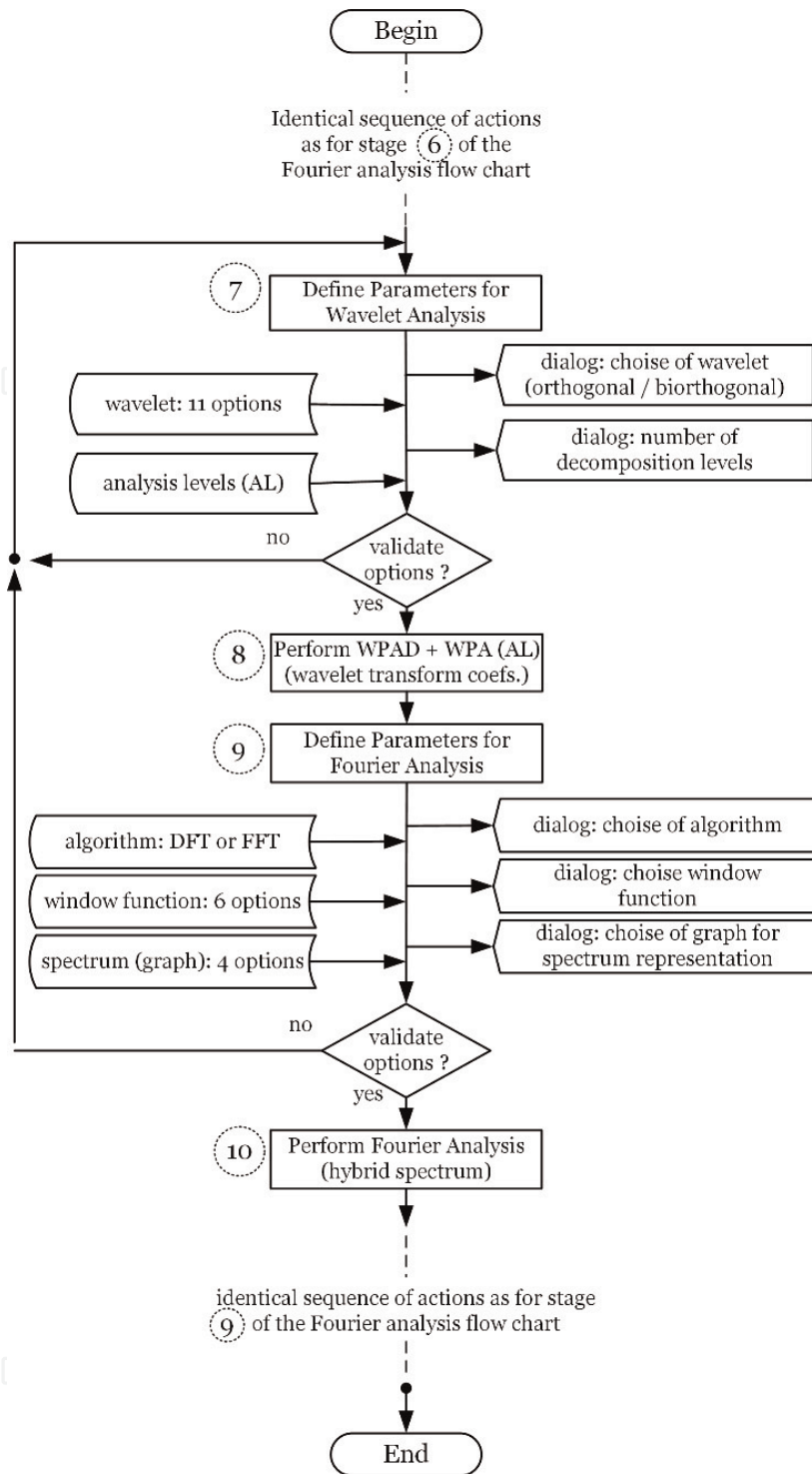


Figure 15. Sequence of action involved in combined wavelet-Fourier analysis.

the wavelet function to use (orthogonal DBn or biorthogonal CDF families), and the number of analysis levels—ALs.

If these parameters are valid, a one-level wavelet packet analysis and denoising (WPAD) is performed, using the Shannon entropy associated with the signal. The signal is then reconstructed and submitted to WPA using the wavelet function specified with AL decomposition levels [16]. As a consequence, the wavelet transform coefficients are organized in frequency sub-bands, as shown in **Figure 12**. The bandwidth in each sub-band is established by dividing the Nyquist bandwidth by a factor expressed as a power of two, such that $r = 2^{AL}$. Then, the wavelet coefficients in sub-bands are submitted to Fourier analysis to obtain the hybrid wavelet-Fourier spectrum [17].

The Normalized Cross-Correlation (NCC) is a traditional technique to evaluate the resemblances between two signals, expressed as

$$\|r_{sy}[l]\| = \frac{r_{sy}[l]}{\sqrt{r_{ss}[0] \cdot r_{yy}[0]}}, \quad (21)$$

for discrete-time signals $s[n]$ and $y[n]$. Here, $r_{ss}[0]$ and $r_{yy}[0]$ represent the auto-correlation of these signals with null lag, and $r_{sy}[l]$ the cross-correlation coefficients with lag l , defined as

$$r_{sy}[l] = \sum_{n=-\infty}^{\infty} s[n] \cdot y[n-l], \quad l = 0, \pm 1, \pm 2, \dots, \quad (22)$$

The NCC supports the evaluation of spectral similarities of the audio signals emitted for two different configurations of the LSRA, considering the amplitude spectrum coefficients and a given frequency lag.

Another method to estimate the spectral similitudes is the Cross-Power Spectrum Density (CPSD) which corresponds to the DFT of the cross-correlation (Eq. (22)). The CPSD is expressed as

$$S_{sy}[l] = \frac{1}{N} \sum_{n=0}^{N-1} r_{sy}[n] \cdot e^{-j\frac{2\pi nl}{N}} = R_{sy}[l] \cdot e^{-j\phi_{sy}[l]}, \quad (23)$$

where $R_{sy}[l]$ and $\phi_{sy}[l]$ are, respectively, the amplitude cross-spectrum and the phase cross-spectrum. The CPSD is estimated via the Welch periodogram [18].

5. Experimental characterization and results of local responses

To characterize the vibrations of the LSRA through experimental methods, we established a test setup to conduct a set of tests for experimental modal excitation and for operational modal analysis. For these tests and according to the instrumentation configuration, we collected data of the local accelerations and recorded the audio emitted. For that purpose, during the tests, the actuator remained inside of a semi-anechoic chamber [19].

5.1 Results from experimental modal excitation

For any excitation point of **Figure 9**, a set of tests were performed for each configuration, the local accelerations are measured, and the audio recorded is analyzed to obtain its spectral components. The overabundance of results leads to a quite exhaustive analysis; therefore, only a few examples are presented here. **Figures 16** and **17** show the amplitude spectrum of the audio signals for configurations P1 and P2, respectively, both obtained for a steady-state sinusoidal force of 4.5 N applied at E1 (see **Figure 9**), and linear frequency variation from 10 Hz to 1.3 kHz.

Both Figures reveal prominent amplitude peaks at 65 Hz, which correspond to the first mode for P1 and P5 (dual configurations). The nearest peaks at the right-hand side have a frequency near 75 Hz and correspond to the first mode in positions P2 and P4. The 180- and 201-Hz frequency components are related to modes 12 and 13, respectively, and the frequencies of 282 and 290 Hz are connected to mode 19.

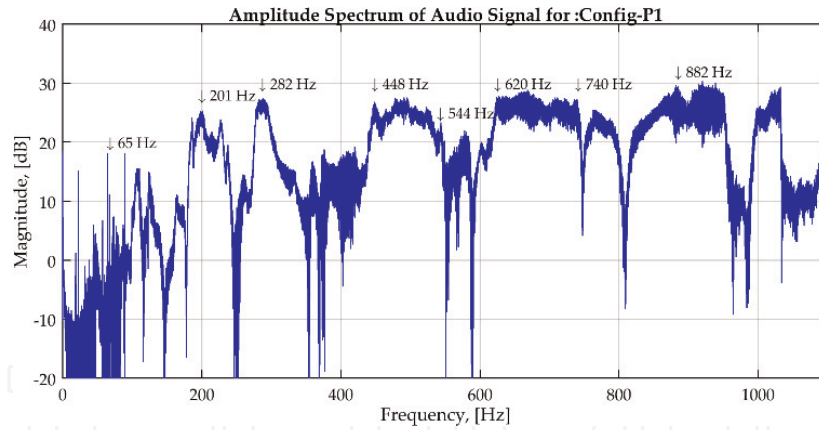


Figure 16.
Spectral components relative to modal frequencies excited at P1.

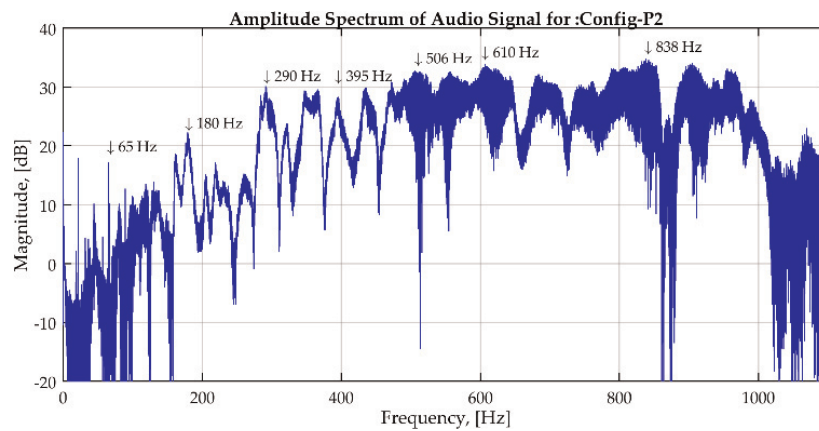


Figure 17.
Spectral components relative to modal frequencies excited at P2.

The range of frequencies around 610/620 Hz corresponds to the modal frequencies of modes 40–44.

Moreover, the highlighted frequencies, 838 and 882 Hz, are linked to vibrations almost exclusively at the primary circuit's parts. The deviations among the experimental results and the values obtained via FEM are due to non-ideal contacts and tolerances present at the real actuator. Still, the test data results are coherent and close to those obtained by numerical methods.

5.2 Characterization for operational modal excitation

For the experimental evaluation of the local vibrations produced with the LSRA in operation, we consider the test setup referred in subsection 4.1, and configuration P2. The switching frequency f_{Ta2} is set to 465 Hz and duty cycle to 85%, obtaining an average current of 1.3 A and a traction force of ~ 30 N [20]. To evaluate the vibrations due to operation using these conditions, we take modes #30-P2 (444 Hz) and #33-P2 (487 Hz) as references. On one side, the value of the switching frequency is in between the values of the two natural frequencies obtained from FEM and corresponding to these two modes. On the other side, the modal shapes associated with these modes reveal transverse displacements along the vertical direction, as shown in **Figures 18** and **19**, respectively. The modes with deflections through the vertical direction are relevant for this analysis. Mode #67-P2 (976 Hz) is also pertinent for analysis as its frequency corresponds to the first

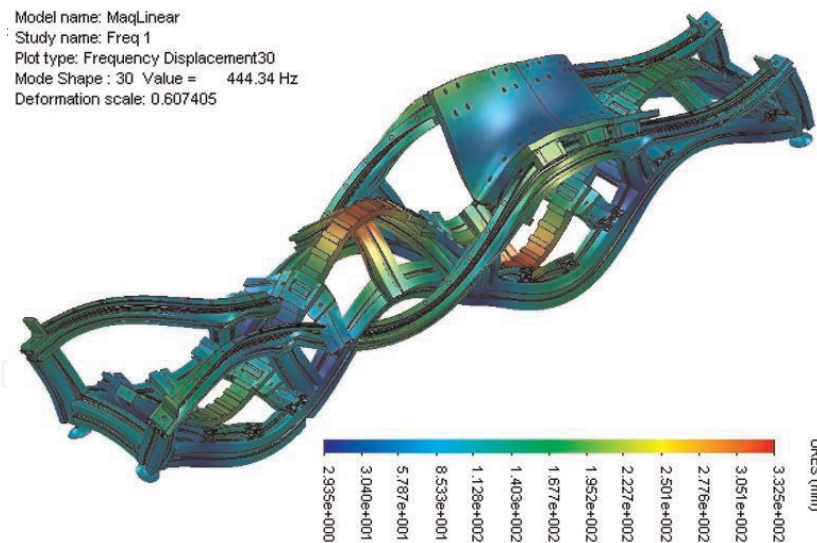


Figure 18.
 Details of the modal shape related to mode #30 for configuration P2.

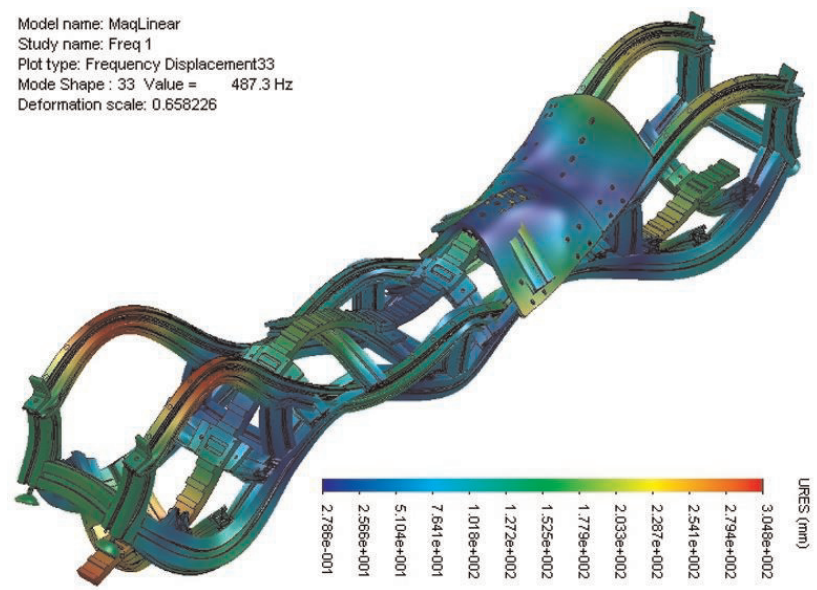


Figure 19.
 Details of the modal shape related to mode #33 for configuration P2.

harmonic of f_{Ta2} , and its modal shape denotes movement almost exclusively at the secondary of the actuator, as shown in **Figure 20**.

The peaks of deformation in the modal shapes for configuration P2 are almost coincident with the positions considered for measuring the local responses (see **Figure 10**). Among these points, we refer mainly to SF1, SP1, SS1, SS2, and STz (see **Figures 18–20**). The characteristics above mentioned highlight the potential of excitation of these modes under operation, thus turning these test conditions into a good example and representative case for analysis.

Figures 21 and 22 show the time representation of the signal controlling switch, T_{a2} , measured with an oscilloscope probe, and the current through phase a , i_{as} , measured via a ratiometric current sensor (voltage output), respectively.

Observing **Figure 22**, we verify that the waveform of the AC component of the phase current (almost triangular) and two frequencies are visible at the amplitude spectrum: one at 464 Hz and the other one at 933 Hz (first harmonic). These frequency components are as expected and coherent with the switching frequency

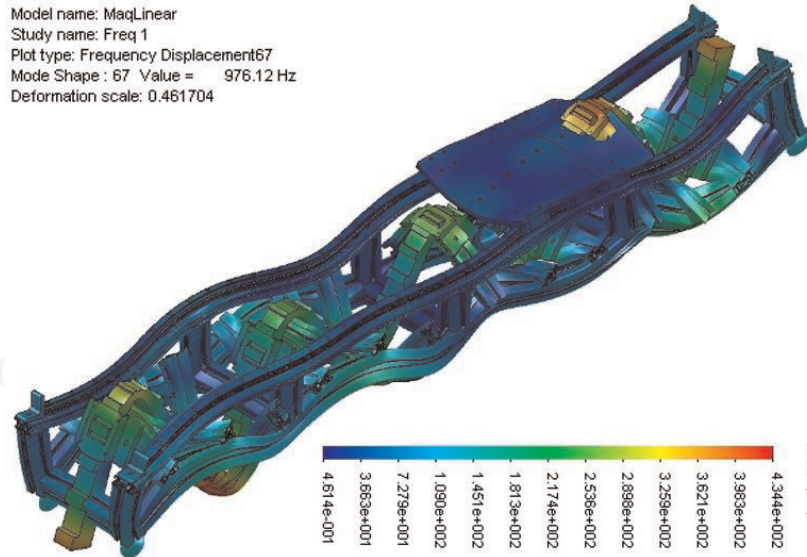


Figure 20.
 Details of the modal shape related to mode #67 for configuration P2.

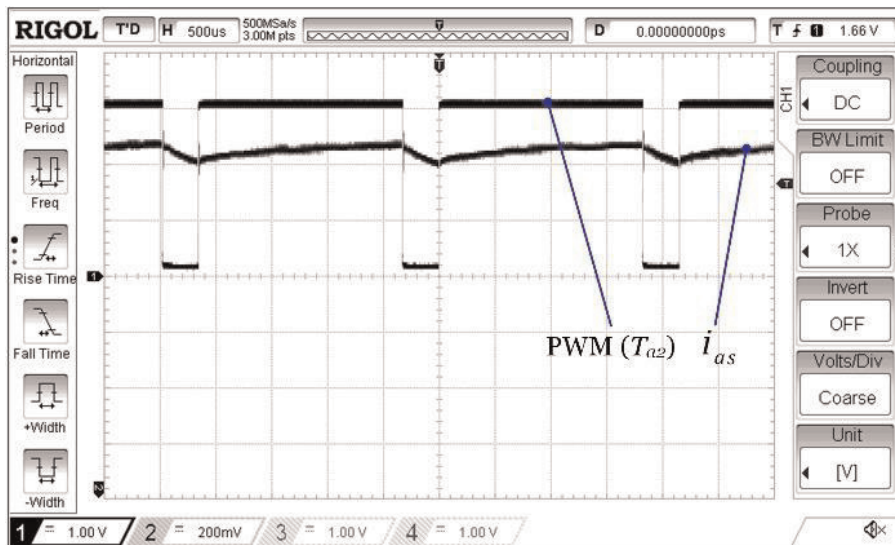


Figure 21.
 Waveforms of the current through phase a and of control signal T_{a2} (PWM).

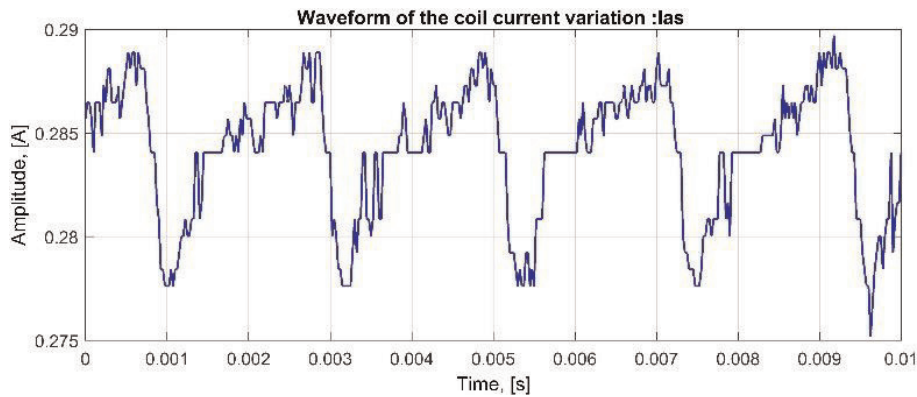


Figure 22.
 Waveform related to the AC component of the current in phase a.

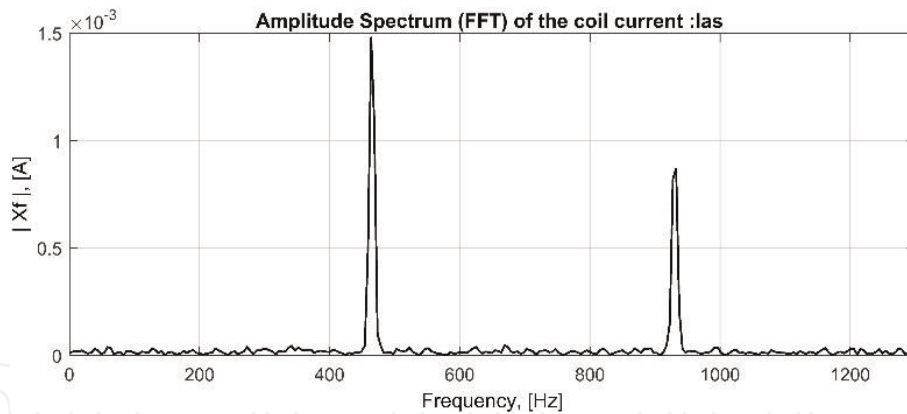


Figure 23.
Spectral components from the analysis of the current in phase a.

used to control the excitation, and the amplitude of the harmonic is coarsely half of that of the primary frequency.

Figure 23 presents the harmonic analysis of the phase current using the windowed fast Fourier transform (FFT) using the Hann window. The resulting amplitude spectrum considers the band up to 1300 Hz (frequencies of interest). From Eqs. (5)–(7), we can expect ripple in the forces generated in the actuator, which influences these two frequency components. Therefore, for a 5% error margin, the ripple in the electromagnetic forces and their interactions have the potential to excite the natural modes considered as reference.

The local vibrations caused by the action of the attraction and thrust forces are evaluated through the response of the accelerometers placed at the structure. We consider mostly the vibrations with vertical displacement at the platforms associated with the primary, and at the bar forming the secondary of the actuator. The frequency analysis of the local accelerations is also performed through the FFT using the Hann window. We start by probing the local responses measured at the points in **Figure 10** that are located close to the primary and the secondary of the actuator.

The accelerometer at the top of the platforms measures the responses along the three axes: X (longitudinal), Y (transverse), and Z (vertical). Among these, the acceleration along the Z-axis is of singular interest for analysis. The time evolution of its signal is shown in **Figure 24** and resembles the waveform of the phase current in **Figure 22**. This is related to the phase coils of the primary, which are assembled just below the top platforms. The ripple is mainly related to the attraction force and is straightly perceived with peak values of acceleration at $+0.6$ and -1 ms^{-2} .

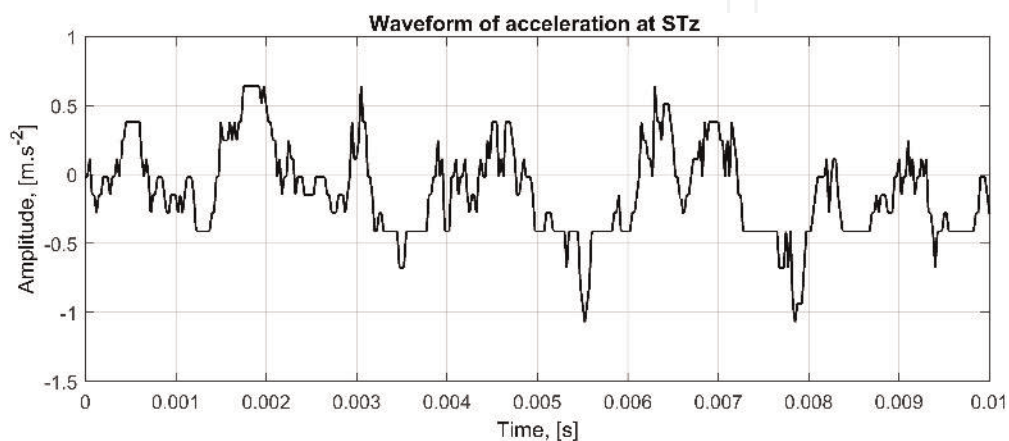


Figure 24.
Time evolution of the local accelerations along the Z-axis at STz.

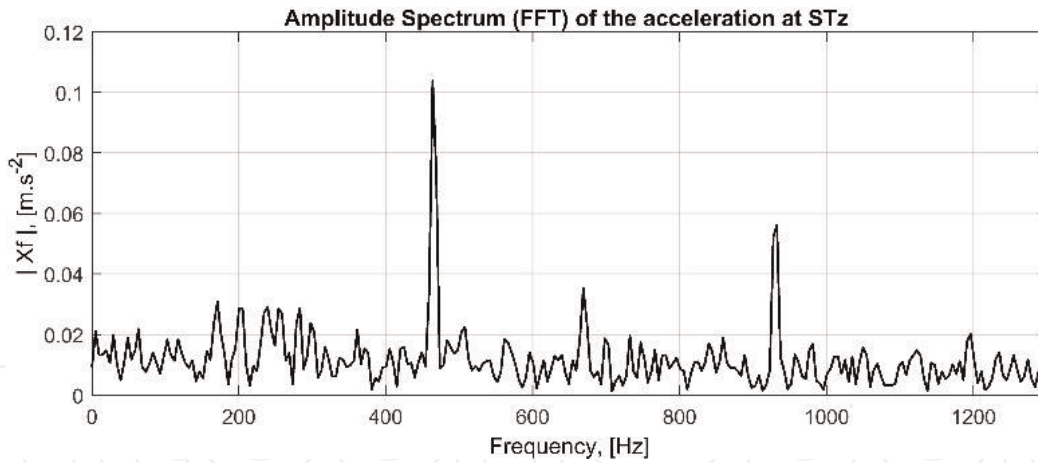


Figure 25.
Spectral components associated with the acceleration at STz.

Figure 25 shows the amplitude spectrum of the acceleration measured through STz with spectral components equivalent to the current. A less significant component around 669 Hz also appears which is related to modes considered exclusively associated with vibrations at the primary, as its frequency is almost constant regardless of the position of the translator.

Figure 26 presents the time evolution of the acceleration measured at SS1 (bar of the secondary), showing peak values reaching $\pm 20 \text{ ms}^{-2}$, which are higher than those obtained for STz. Two main reasons explain this: (1) the proximity of SS1 to the air gap where the forces are generated and (2) the higher value of stiffness associated to the material of the secondary bar (steel vs. aluminum).

The spectrum of accelerations at SS1 shown in **Figure 27** reveals frequency components with higher values than those obtained in the previous case, which is confirmed by its amplitude spectrum.

Besides the spectral components at 464 and 928 Hz, which are familiar to the spectrums of SS1 and STz, it exposes frequency components at 869 Hz (#56-P2 ~ 858 Hz), 1050 Hz (#72-P2 ~ 1055 Hz), and 1143 Hz (#76-P2 ~ 1141 Hz). All these frequencies correspond to modal shapes of configuration P2 that present displacements along the bar of the secondary.

The homologous spectrum at SS2, shown in **Figure 28**, presents similar frequency components as in SS1, namely the switching frequency, its first harmonic, and component around 1050 Hz. However, in this case, the amplitude values are lower, which is explained by the proximity to the air gap. Besides, two new

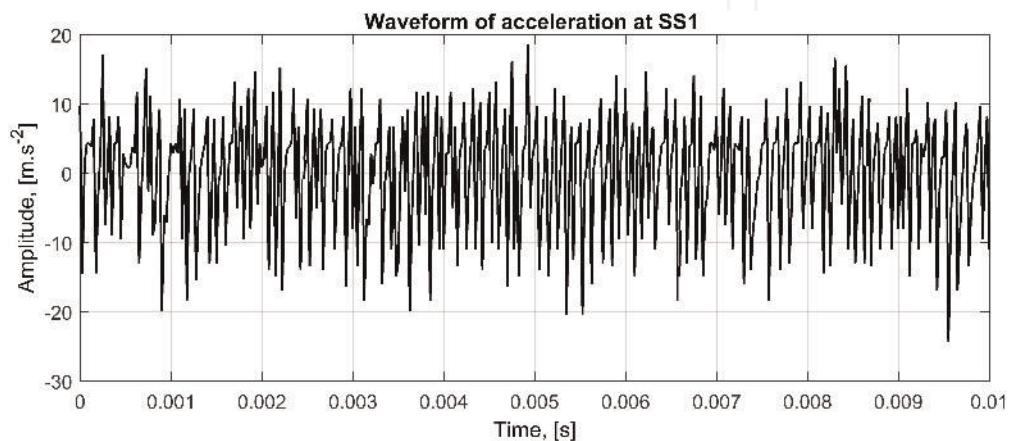


Figure 26.
Time-domain evolution of acceleration along the Z-axis at SS1.

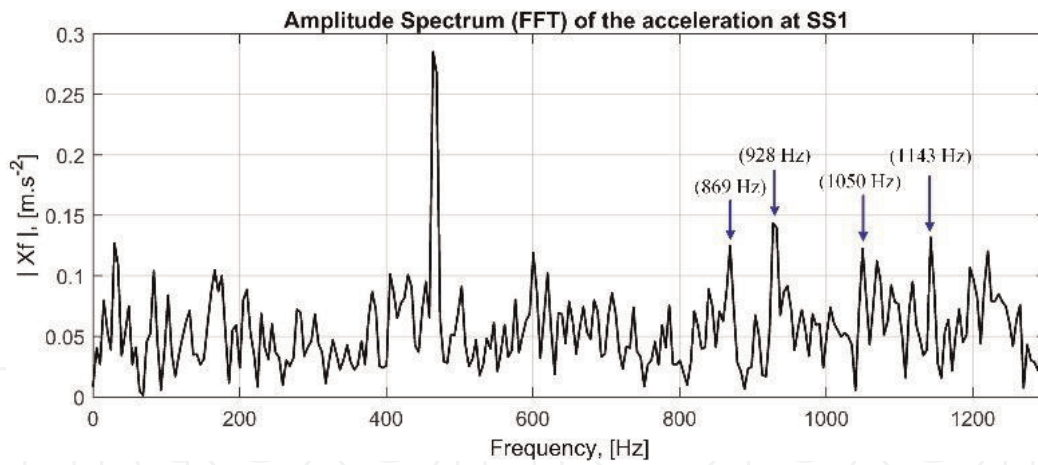


Figure 27.
Spectral components associated with the vertical acceleration at SS1.

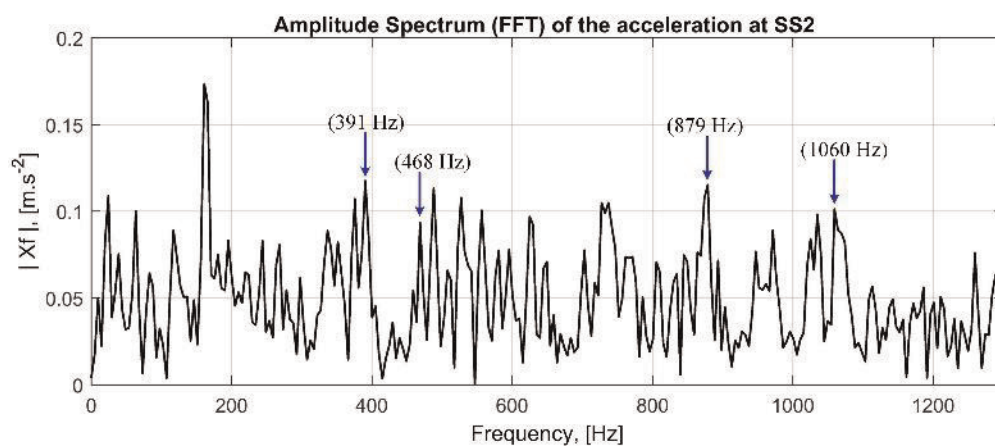


Figure 28.
Spectral components associated with vertical accelerations at SS2.

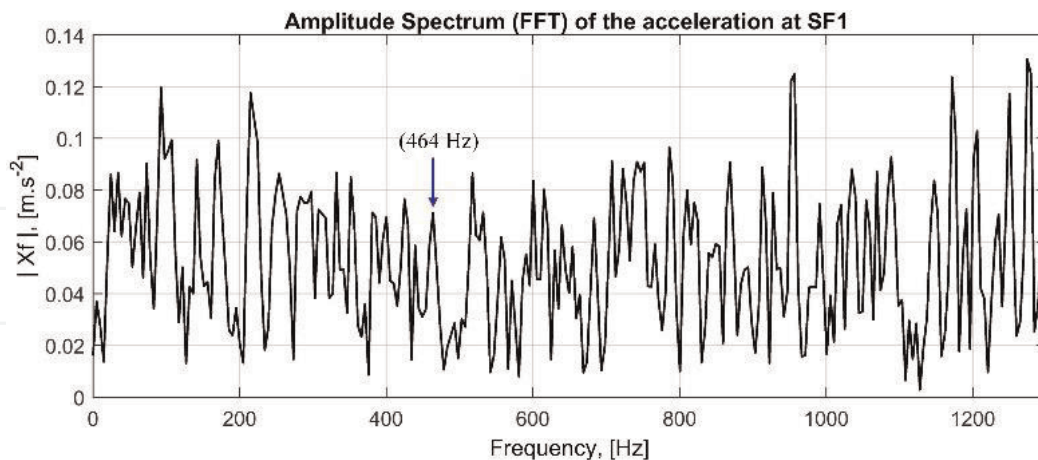


Figure 29.
Spectral components associated with vertical accelerations at SF1.

components are exposed for 161 and 391 Hz, both related to configuration P3, where the first is more significant.

Finally, the amplitude spectrum of the local vibrations measured at SF1 and SF2 reveal a more complex harmonic content, as presented in **Figures 29** and **30**.

We also notice in both cases that the switching frequency is not the most relevant component and that the number of modes excited with a single frequency is significant. For SF1, the frequency components with an amplitude equal to or

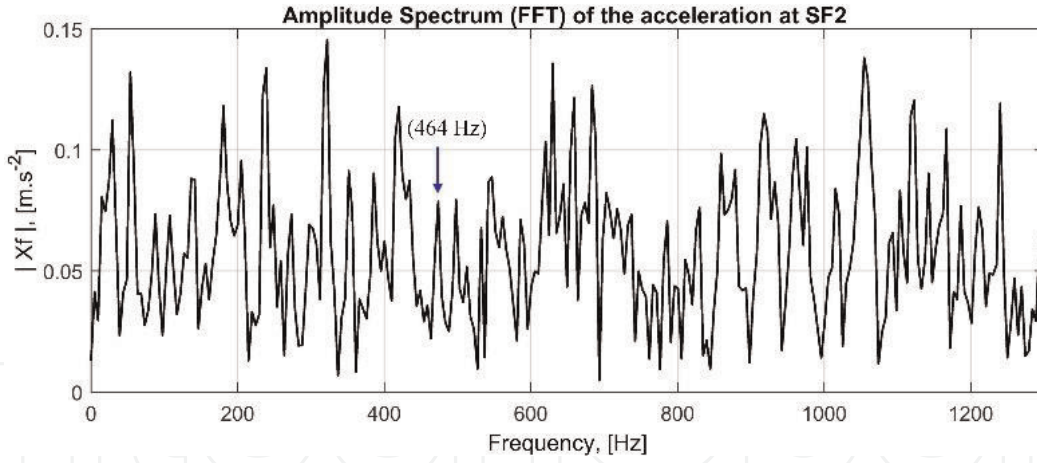


Figure 30.
Spectral components associated with vertical accelerations at SF2.

greater than 0.1 ms^{-2} are (in Hz): 93, 215, 957, 1172, and 1274. For SF2, the components with amplitude equal to or greater than 0.12 ms^{-2} are (in Hz): 53, 239, 322, 630, 660, 684, 918, 1055, 1123, and 1240. Two reasons explain these phenomena: first, the number of degrees of freedom for movement at the top longitudinal bars is greater, due to the absence of other parts assembled transversely; second, the influence of elastic wave propagation, or transmission, with origin in vibrations from other parts. These features demonstrate the potential to excite multiple modal frequencies with a single switching frequency during the power converter operation.

6. Spectral analysis of the audio emitted

The spectral signature that characterizes the LSRA vibrations can also be identified by analysis of the audio noise emitted during the experimental tests [21]. The audio is recorded in “wave” file format (*.wav) with a sample rate of 22,050 sa/s represented with 16 bits per sample. The tests consist of coupling an electrodynamic shaker to structure and apply transverse forces at the excitation positions defined in **Figure 9**. The intensity of the forces is fixed while its frequency varies linearly from 10 to 1300 Hz. These forces (sinusoidal) excite essentially the frequencies whose mode shapes represent transverse deformations along the horizontal direction. The symmetry characteristics suggest that the pairs E1-P2, E2-P2, E3-P4, and E4-P4 can be considered as representatives of the natural vibrations of the actuator.

Figures 31 and **32** represent the NCC of the amplitude spectrums of the audio signal considering the similarities of the following excitation-configuration pairs: E1-P2, E2-P2, E3-P4, and E4-P4.

Concerning the symmetric excitation pairs, the similarities are higher than 95% for frequency deviations up to 6 Hz, 90% for $\Delta f \in [-27, +10]$ Hz, and 80% for $\Delta f \in [-41, +20]$. For the anti-symmetric pairs, and using similar values of the frequency lag, the maximum likeness is 84.5% for the normalized cross-correlation considering E1-P2 vs. E4-P4 and 75.2% for E2-P2 vs. E3-P4. The NCC reduces to 70% for frequency deviations near ± 40 Hz. These values of NCC confirm the quasi-symmetric characteristic of the actuator.

Figures 33 and **34** show the spectral resemblances of the audio at configurations P2 and P4, respectively, obtained through the CPSD and considering two excitation points for each configuration. Each graph denotes a total of 28 spectral components, which are considered the main vibration frequencies for each configuration.

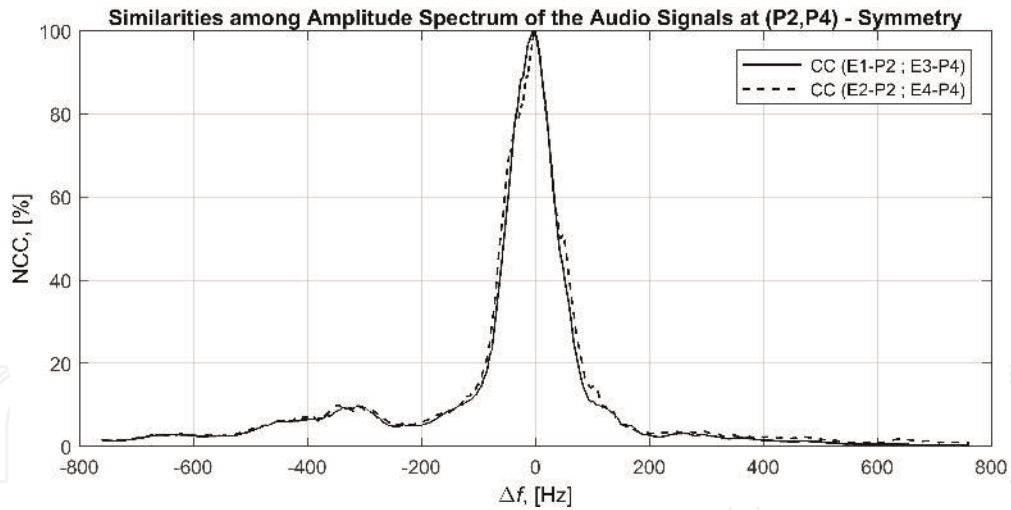


Figure 31.
Normalized cross-correlation relative to the symmetric pairs.

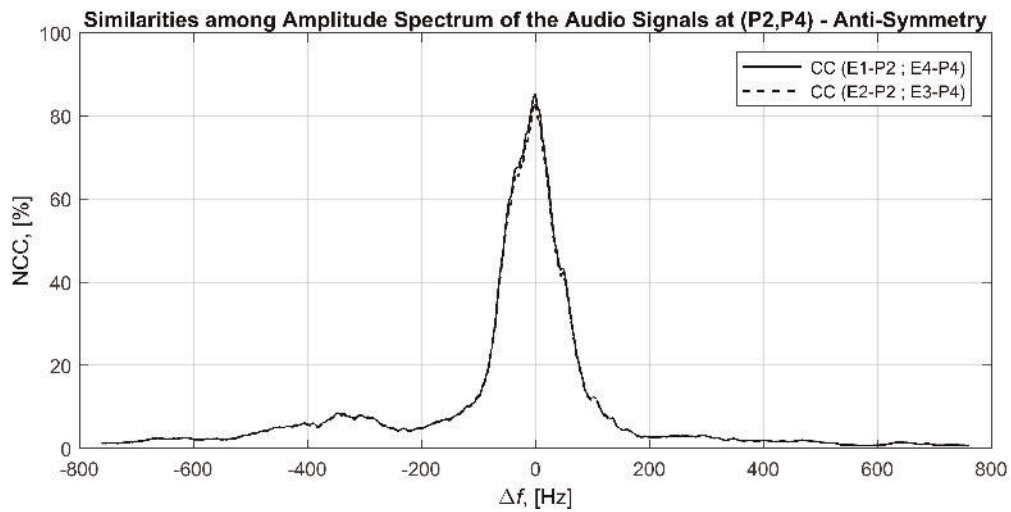


Figure 32.
Normalized cross-correlation relative to the anti-symmetric pairs.

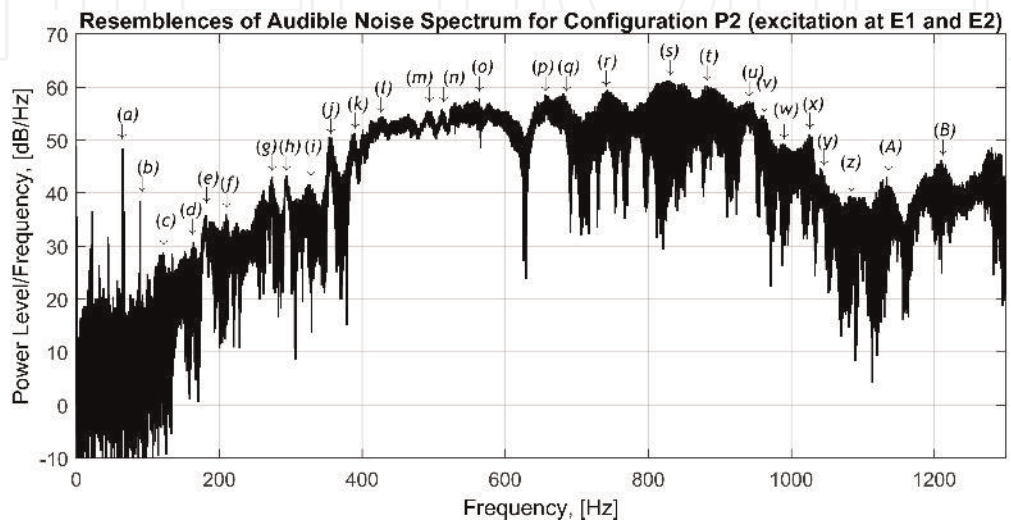


Figure 33.
Similarities among frequency components at P2 (CPSD and FFT).

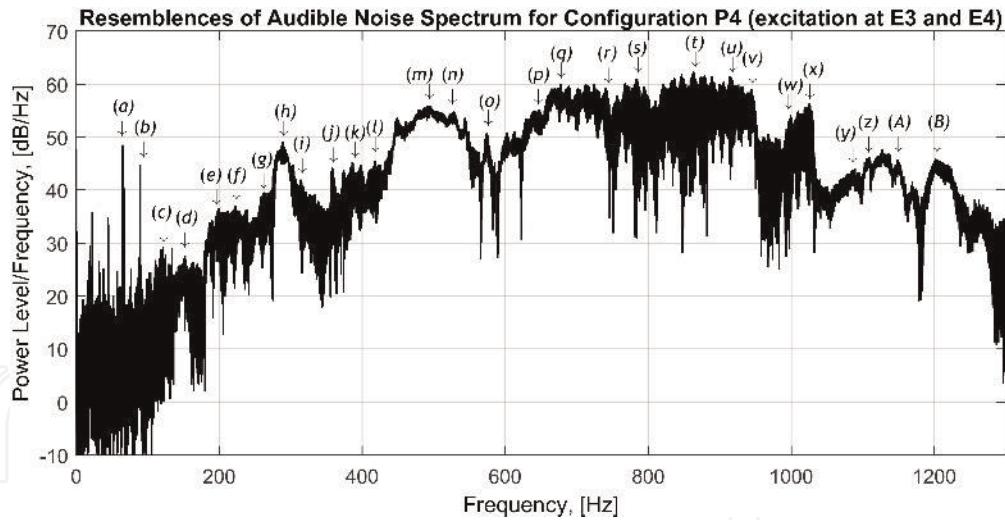


Figure 34. Similarities among frequency components at P4 (CPSD and FFT).

Figures 35 and 36 show the hybrid spectrum of the audio signals at E1-P2 and E2-P2, respectively, obtained as described in the flowchart of Figure 15, using biorthogonal 4.4 wavelets for WPA with three levels of analysis. The resulting DWT coefficients are organized in sub-bands with 1.38 kHz bandwidth, corresponding to the frequencies of interest (~1.3 kHz).

The similarities between the amplitude hybrid-spectrum for E1-P2 and for E2-P2 are noticeable in Figures 35 and 36. Moreover, with these graphs, a total of 40 frequency components are identified, including the 28 components previously recognized and referred for similar configurations. Hence, 12 new frequencies referenced by (+) are perceptible.

Table 1 presents a list of all frequency components recognized through the CPSD and the error values with respect to the results from FEM analysis.

The relative average frequency deviation in Table 1 is 2.67%. Except for the first three spectral components, the relative frequency deviation is, in general, less than 5%. It is important to note that some spectral components have close frequencies, which present difficulties in its identification. That is the case, for example, of component (h) which can be associated either to mode #19 or to mode #20. The same applies to frequency component (p) with respect to modes #45 and #46, and to component (t) and modes #59 and #60, respectively. In observations, (P)

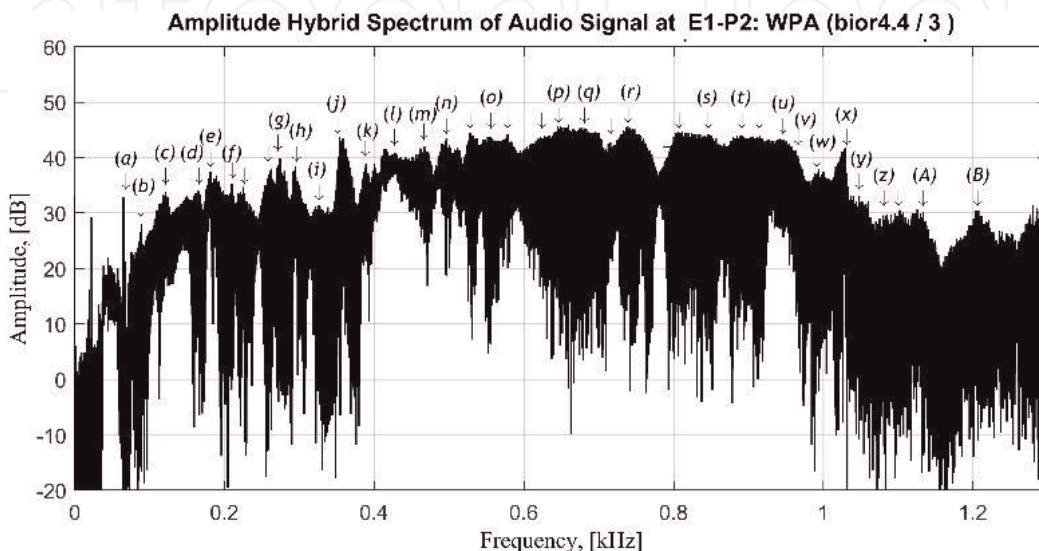


Figure 35. Frequency components' similarities at E1-P2 (wavelet-Fourier).

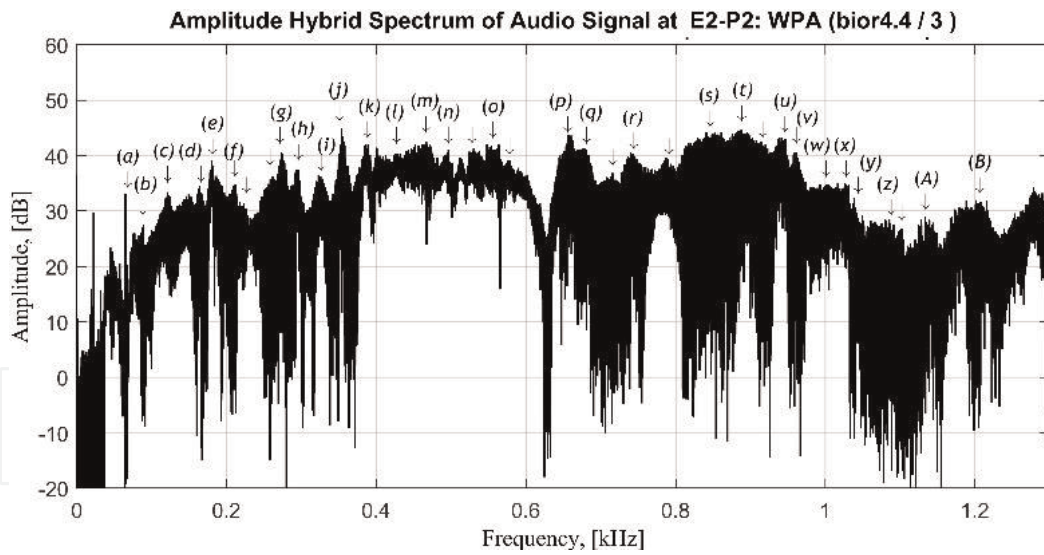


Figure 36.
 Frequency components' similarities at E2-P2 (wavelet-Fourier).

Freq. Comp.	f_n FEM [Hz]	f_n E1 [Hz]	f_n E2 [Hz]	Δf_n av [%]	#mode (FEM)	Obs.
(a)	76	65	65	14.47	7	
(b)		89	89			#7-P3
(c)	133	121	121	9.02	9	
(d)	177	164	164	7.34	10	
(e)	180	181	180	0.28	11	
(f)	201	210	210	4.28	13	
(+)	234	224	224	4.27	15	
(+)	260	262	262	0.77	16	
(g)	266	274	273	2.82	17	
(h)	284	295	296	4.05	19	#20
(i)	325	327	323	0.62	22	
(j)	370	354	354	4.32	25	
(k)	387	389	386	0.39	26	
(+)	394	400	400	1.52	27	(P)
(+)	413	415	413	0.24	28	(P)
(l)	420	429	427	1.91	29	
(m)	460	467	467	1.52	32	
(n)	496	496	497	0.10	34	
(+)	528	528	530	0.19	35	
(o)	552	555	554	0.45	38	
(+)	568	578	578	1.76	39	
(+)	639	648	NI	1.41	44	
(p)	665	660	657	0.98	45	#46
(q)	681	684	678	0.44	47	
(+)	722	726	717	0.62	49	

<i>Freq. Comp.</i>	f_n FEM [Hz]	f_n E1 [Hz]	f_n E2 [Hz]	Δf_n av [%]	#mode (FEM)	<i>Obs.</i>
(r)	751	739	740	1.54	51	
(+)	790	805	787	1.14	54	torsion
(s)	855	850	849	0.64	55	(P)
(t)	885	890	888	0.45	60	#59
(+)	908	913	914	0.61	62	#63
(u)	933	943	942	1.02	65	
(v)	960	963	961	0.21	66	hidden
(w)	983	994	1004	1.63	69	
(x)	1032	1028	1027	0.44	71	
(y)	1055	1048	1039	0.96	72	
(z)	1085	1085	1086	0.04	73	
(+)	1096	1102	1103	0.59	75	
(A)	1153	1145	1134	1.17	77	
(B)	1196	1208	1202	0.75	79	#78

Table 1.
List of vibration frequencies identified by the wavelet-Fourier analysis.

denotes modes relative to vibration frequencies associated with deformations exclusively located to the primary circuit parts.

These results show that the wavelet-Fourier approach allows a gain of 42.86% for frequency components identification with respect to the CPSD. Moreover, with the wavelet-Fourier analysis, both the magnitudes and the relevance of each component become more evident, as shown by comparing **Figures 33** and **35** and taking components (*j*), (*k*), and (*m*) as reference.

The hybrid spectrum representations for configuration pairs E3-P4 and E4-P4 reveal similar results like the ones obtained for P2. These features demonstrate the effectiveness of this approach for the identification and characterization of the vibrations in the LSRA. The wavelet-Fourier method can also be used for audio signals collected during the tests of operational modal excitation of the actuator, as shown in **Figure 37**, using the 4.4 biorthogonal wavelets with three levels of analysis.

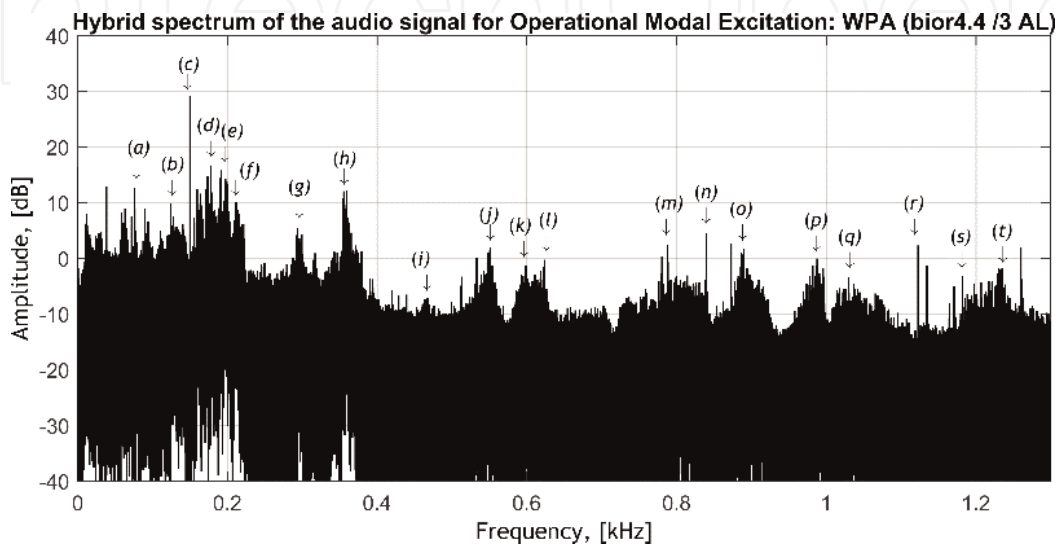


Figure 37.
Frequency components identified by wavelet-Fourier analysis of the audio emitted during the experimental tests.

Among the components identified, the following relations with natural modes are possible: (*f*) relates to mode #14, (*n*) links to both modes #55 or #56, (*p*) is related to modes #67 or #68, and (*r*) corresponds to mode #74. These results are related to those obtained by FEM analysis whose modal shapes denote transverse movement along the vertical direction, and those with displacements almost exclusively located at magnetic circuit parts.

7. Conclusion

This chapter describes a research work aimed to evaluate and characterize the vibrations in a three-phase LSRA. The actuator is described in terms of its structure and according to its modes of operation.

To analyze and evaluate the structural vibrations, we built the 3D mechanical model and performed numerical simulations using the finite element method and iterative methods to find the solution of the system dynamics. The natural frequencies obtained and the corresponding mode-shapes support the characterization of the vibrations at the actuator for both, external forces applied or forces developed during the operation of the actuator. The numerical evaluation of the natural frequencies considers five configurations of the actuator, according to the position of its platforms. For each configuration, a total of 74 modal frequencies are considered in the range up to nearly 1.3 kHz. Besides the frequency values, the mode shapes, associated with each mode, are also crucial for analysis as they evidence the parts with relevant deformations. Owing to the complexity of the LSRA structure and its symmetry characteristics, in general, the vibration frequencies, and the mode shapes are related for configurations corresponding to dual positions.

An experimental setup for the evaluation of the vibrations is also proposed, including the test bench configuration and the instrumentation set used to permit a collection of data results, showing the most relevant modal frequencies associated with the LSRA operation. The data acquisition system and the analysis tools were developed specifically for this research.

In addition to experimental modal excitation, operation modal excitation tests were also performed to identify the potential of excitation of the natural modes, and the critical values for the switching frequency. The operational responses produced, either the phase current or the local acceleration, were measured and evaluated. The spectral components related to these quantities at the selected points were analyzed and discussed regarding the results from FEM analysis. Besides Fourier analysis, a tool performing a combined wavelet-Fourier analysis of signals through a wavelet packet decomposition was also developed, proposed, and evaluated with quality improvements to the identification of the frequency components.

The results of the hybrid spectrum representation demonstrate the reliability and suitability of the wavelet-Fourier approach. The Normalized Cross-Correlation and the spectrum coherence using the Cross-Power Spectrum Density were also used. Moreover, the spectrum of the audio signals emitted was collected and analyzed, serving to confirm the data obtained by the simulation and supporting the experimental characterization of the actuator.

The results obtained are consistent and agree with the analytical estimations obtained through FEM simulations and confirm the experimental results of modal excitation obtained by experimental methods.

The data collected allow establishing a framework to fully characterize the linear actuator, regarding the vibration modes due to its regular operation, and to identify the vibration modes that can be excited for different positions of the actuator's moving parts. The information gathered serves also to improve the actuator's

control by avoiding excitation regimes with frequencies near its natural vibration frequencies. That also permits to modify the structural configuration of the actuator aiming for low vibrations, either by choosing the right materials for the critical parts or by adopting suitable mechanical project strategies to redesign the structure of the actuator to avoid sensitive vibration frequencies.

Acknowledgements

The authors wish to thank Instituto de Telecomunicações for funding this work, with the investigation scholarship UID/EEA/50008/2019.

Nomenclature

c_r, m_r, k_r	damping, mass and stiffness coefficients for mode r
$\mathbf{C}, \mathbf{K}, \mathbf{M}$	matrices of generic damping, mass, and stiffness coefficients
$\mathbf{C}_r, \mathbf{K}_r, \mathbf{M}_r$	matrices of damping, mass, and stiffness for mode r
D_R	Rayleigh dissipation function
f_{ea}, f_{em}, f_{er}	electromagnetic attraction, motoring, and regenerative forces
i_{as}, L_{as}	coil excitation current and inductance of phase a
Q_i, \mathbf{Q}_i	generalized non-conservative forces (scalar and matrix forms)
$r_{sy}[l]$	cross-correlation of discrete-time signals $s[n], y[n]$ with lag l
$R_{sy}(l)$	the cross-spectrum amplitude of discrete-time signals $s[n], y[n]$
S_{sy}	cross-power spectrum density of discrete-time signals $s[n], y[n]$
$S_w[k]$	discrete Fourier transform of $s[n]$ for discrete window $w[n]$
v_{La}	electromotive force induced at the coil of phase a
$x_i, \dot{x}_i, \ddot{x}_i$	displacement, velocity, and acceleration at generic coordinate i
$\mathbf{x}_i, \dot{\mathbf{x}}_i, \ddot{\mathbf{x}}_i$	vectors of displacement, velocity, and acceleration at coordinate i
x_m	longitudinal displacement (position)
W_{em}	electromagnetic energy stored in the coupling field
W_{kin}	kinetic energy stored in the mechanical system
W_{pot}	potential energy stored in the mechanical system
$\phi_{sy}(l)$	phase cross-spectrum of signals $s[n], y[n]$ with lag l
λ_{as}	flux linkage in phase a (for values of i_{as} and L_{as})
ξ_r, Ψ_r	eigenvalue and eigenvector relative to natural mode of order r
ω_r	undamped angular natural frequency of mode r

IntechOpen

Author details


José António da Costa Salvado^{1*}, Maria do Rosário Alves Calado² and António Eduardo Vitória do Espírito-Santo²

1 School of Technology, Polytechnic Institute of Castelo Branco, Castelo Branco, Portugal

2 Faculty of Engineering, Instituto de Telecomunicações and University of Beira Interior, Covilhã, Portugal

*Address all correspondence to: josesalvado@ipcb.pt

IntechOpen

© 2020 The Author(s). Licensee IntechOpen. Distributed under the terms of the Creative Commons Attribution - NonCommercial 4.0 License (<https://creativecommons.org/licenses/by-nc/4.0/>), which permits use, distribution and reproduction for non-commercial purposes, provided the original is properly cited. 

References

- [1] Castano SM, Bilgin B, Fairall E, Emadi A. Acoustic noise analysis of a high-speed high-power switched reluctance machine: Frame effects. *IEEE Transactions on Energy Conversion*. 2016;**31**(1):69-77
- [2] Furqani J, Kawa M, Kiyota K, Chiba A. Current waveform for noise reduction of switched reluctance motor in magnetically saturated condition. In: 2016 IEEE Energy Conversion Congress and Exposition (ECCE). 2016;**54**(1): 213-222
- [3] Bayless J, Kurihara N, Sugimoto H, Chiba A. Acoustic noise reduction of switched reluctance motor with reduced RMS current and enhanced efficiency. *IEEE Transactions on Energy Conversion*. 2016;**31**(2):627-636. Available from: <http://ieeexplore.ieee.org/document/7349203/>
- [4] Ma C, Qu L, Mitra R, Pramod P, Islam R. Vibration and torque ripple reduction of switched reluctance motors through current profile optimization. In: 2016 IEEE Applied Power Electronics Conference and Exposition. Long Beach, CA, USA: IEEE; 2016. pp. 3279-3285. Available from: <http://ieeexplore.ieee.org/document/7468336/>
- [5] Mollet Y, Gyselinck J, Sarrazin M, Van Der Auweraer H. Experimental noise and vibration analysis of switched reluctance machines comparison of soft and hard chopping in transient conditions. In: 2015 International Conference on Renewable Energy Research and Applications. Palermo: IEEE; 2015. pp. 420-425. Available from: <http://ieeexplore.ieee.org/document/7418448/>
- [6] Krishnan R. Switched Reluctance Motor Drives: Modeling, Simulation, Analysis, Design, and Applications. Industrial Electronics. Boca Raton, FL: CRC Press; 2001
- [7] Mohanty P, Rixen DJ. Identifying mode shapes and modal frequencies by operational modal analysis in the presence of harmonic excitation. *Experimental Mechanics*. 2005;**45**(3):8
- [8] Espírito-Santo AE, Calado MRA, Cabrita CMP. On the influence of the pole and teeth shapes on the performance of linear switched reluctance actuator. *COMPEL—The International Journal for Computation and Mathematics in Electrical and Electronic Engineering*. 2011;**30**(2): 412-430. Available from: <http://dx.doi.org/10.1108/03321641111101005>
- [9] Barnes M, Pollock C. Power electronic converters for switched reluctance drives. *IEEE Transactions on Power Electronics*. 1998;**13**(6):1100-1111. DOI: 10.1109/63.728337
- [10] Meirovitch L. Fundamentals of Vibrations. Boston: McGraw-Hill; 2001
- [11] Schwarz B, Richardson M. Proportional damping from experimental data. The Conference Proceedings of the Society for Experimental Mechanics Series. 2014; **45**(7):179-186
- [12] Salvado J, Calado M do R, Santo AE, Guerman A. Numerical modal analysis of vibrations in a three-phase linear switched reluctance actuator. *Modelling and Simulation in EngineeringModel*. 2017;**2017**:1-18. Available from: <https://www.hindawi.com/journals/mse/2017/3258376/>
- [13] Salvado J, Espírito-Santo A, Calado M. An intelligent sensor array distributed system for vibration analysis and acoustic noise characterization of a linear switched reluctance actuator. *Sensors (Basel)*. 2012;**12**(6):7614-7633. Available from: <http://www.pubmedcentral.nih.gov/articlerender.fcgi?artid=>

3435993&tool=pmcentrez&rendertype=abstract

[14] Salvado J, Espirito Santo A, Calado MRA. Improved distributed system for analysis of vibrations in linear switched reluctance actuators. In: ICIT 2012, IEEE International Conference on Industrial Technology. Athens: IEEE; 2012. pp. 991-996. Available from: <http://ieeexplore.ieee.org/xpl/articleDetails.jsp?arnumber=6210068&newsearch=true&searchWithin=%22First Name%22:Jose&searchWithin=%22Last Name%22:Salvado>

[15] Wickramarachi P, Corporation DP, Jose S. Effects of windowing on the spectral content of a signal. *Sound and Vibration*. 2003;37(1):10-11. (ISSN 15410161)

[16] Bianchi D, Mayrhofer E, Gröschl M, Betz G, Vernes A. Wavelet packet transform for detection of single events in acoustic emission signals. *Mechanical Systems and Signal Processing*. Elsevier; 2015;64-65:441-451. DOI: 10.1016/j.ymsp.2015.04.014

[17] Tarasiuk T. Hybrid wavelet-Fourier spectrum analysis. *IEEE Transactions on Power Delivery*. 2004;19(3):957-964. Available from: <http://ieeexplore.ieee.org/lpdocs/epic03/wrapper.htm?arnumber=1308314>

[18] Akçay H. Spectral estimation in frequency-domain by subspace techniques. *Signal Processing*. Elsevier. 2014;101:204-217. DOI: 10.1016/j.sigpro.2014.02.015

[19] Salvado JA, Calado MR, Santo AE. A simple yet effective semi-anechoic chamber for the acoustic characterization of an LSRA. *IEEE Latin America Transactions*. 2013;11(5): 1190-1200

[20] Salvado JA, Calado MR, Santo AE. Evaluation of the operational modal

responses in linear switched reluctance actuators. In: 2018 IEEE International Conference on Environment and Electrical Engineering, 2018 IEEE Industrial and Commercial Power Systems Europe (EEEIC/I&CPS Europe). Palermo, Italy: IEEE; 2018. pp. 1-6

[21] Salvado JA, Calado MR, Santo AE. Wavelet-Fourier analysis of audible signals to characterize the vibrations in LSRA. In: 2018 XIII International Conference on Electrical Machines. Alexandroupoli, Greece: IEEE; 2018. pp. 1738-1744